3-13-2017

Southern Ocean Transport by Combining Satellite Altimetry and Temperature/Salinity Profile Data

Michael Kosempa
University of South Florida, mkosempa.au@gmail.com

Southern Ocean Transport by Combining Satellite Altimetry and Temperature/Salinity Profile Data

by

Michael Kosempa

A dissertation submitted in partial fulfillment
of the requirements for the degree of
Doctor of Philosophy in Marine Science
with a concentration in Physical Oceanography
College of Marine Science
University of South Florida

Major Professor: Don Chambers, Ph.D.
Gary Mitchum, Ph.D.
Boris Galperin, Ph.D.
Gregory Johnson, Ph.D.
Joshua Willis, Ph.D.

Date of Approval
February 14, 2017

Keywords: Jason, Argo, Antarctic Circumpolar Current, Transport Dynamics

DEDICATION

For Vali

TABLE OF CONTENTS

LIST OF TABLES

LIST OF FIGURES

ABSTRACT

Zonal geostrophic velocity fields above 1975 dbar have been estimated for the Southern Ocean from 2004 to 2014 based on sea surface topography observed by Jason altimetry and temperature/salinity measured by Argo autonomous floats. The velocity at 1000 dbar estimated has been validated against Argo drift trajectory at the same pressure level available from the Asia Pacific Data Research Center (APDRC). Errors in mapping of dynamic ocean topography, temperature, and salinity have been quantified using the Southern Ocean State Estimate (SOSE). Analysis of errors reveals significant correlations between depth-dependent and –independent contributions to the integrated transport. Further analysis revealed optimal locations of historical ship casts to compliment the transport time series as observed by Argo. Quantifying the error associated with the historical hydrographic section indicated little benefit in combining hydrographic data obtained from ships. The anticorrelation between depth-dependent and –independent contributions was again significant in sampling by ships. The proposed explanation of the anticorrelation in error is underestimation of reference velocity by attenuation and overestimation of depth-dependent transport by attenuation of the velocity shear.

CHAPTER 1:

This research seeks answers to meet the challenges of climate and environmental dynamics and to achieve progress understanding the role of oceans and atmosphere in the climate system and in improving predictive capability for its future evolution. In particular, this research addresses questions of climate dynamics and observation: How is the Antarctic Circumpolar Current (ACC) varying on interannual, decadal, and longer time scales? Do climate variations induce changes in the ACC circulation? How accurately can we measure the time-varying transport of the ACC with modern observational systems?

The Antarctic Circumpolar Current is a unique moderator of Earth's climate system. Its circumpolar extent tranfers properties between basins, connecting the waters of the Indian, Pacific, and Atlantic Oceans. The ACC's divergence brings previously deep water to the surface, separating the subtropical waters of each ocean from the colder waters surrounding Antarctica. Despite its size and importance, understanding the ACC is a challenge. While climate models predict significant changes in ocean transport in a warming world, finding observational evidence of these has been difficult. Increasing winds associated with changes in the Southern Annular Mode are expected to force a response from the Antarctic Circumpolar Current (ACC).

Scientific literature debates the effect of climate change on winds and transport in the Southern Ocean. Large-scale climate models have predicted a poleward movement and strengthening of the westerly winds in the Southern Ocean in a warming world, as well as one with depletion of polar stratospheric ozone, with both effects leading to increased transport and a

southward shift of the Antarctic Circumpolar Current (ACC) [e.g., *Fyfe and Saenko*, 2006; *Gnanadesikan and Hallberg*, 2000]. However, experiments with eddy-resolving models find that increasing westerlies in the Southern Ocean leads to more energetic eddy variability, but no significant trends in transport through the Drake Passage [*Hallberg and Gnanadesikin*, 2006]. Eddy-permitting models predict an "eddy saturation" such that steepening of isopycnals will release the potential energy contained therein as baroclinic eddies [*Hallberg and Gnanadesikan*, 2006, *Meredith et al*. 2012, *Morrison and Hogg*, 2013]. Eddies act to reduce isopycnal steepening and retard transport increases. A study by *Langlais et al.* [2015] found partial eddy saturation where transport and eddy energy both increased over the ACC, which is consistent with the partial eddy saturation predicted by *Farneti et al.* [2010].

These predictions have yet to be directly observed from in situ measurements, primarily due to the problem of observing the ACC's currents at depth. The ACC encircles the Antarctic continent, lacking boundaries at eastern or western sides. A lack of circumpolar boundaries results in significant currents extending deep into the water column such that form drag can balance the work imparted by zonal winds. The traditional observation method relies on limited measurements of precise temperature, salinity (TS) and pressure observations collected by ship casts on transects across the ACC. However, such calculations are limited by the need to know a reference velocity at some level and the lack of that knowledge. *Wunsch and Gaposchkin* [1980] (hereafter WG80) proposed a method in 1980 to resolve the reference velocity problem. It required combining in situ measurements of temperature and salinity with satellite-observed sea surface height (SSH) relative to a geoid.

While WG80 can be applied to local observations, *Wunsch and Gaposchkin's* [1980] promise of ongoing observation of tranpsort across entire basins required observational accuracy,

precision, and coverage not available until recently. The fulfillment of this promising technique requires not only ongoing altimeter measurements, but also a geoid accurate over the entire study area. The supplementary subsurface temperature, salinity and pressure observations also required a spatial and temporal coverage unavailable until the 21st century. Prior to advances in satellite observation and the Argo program, observations of the Southern Ocean were especially sparse and suffered from a seasonal bias. Today, the data required to implment WG80 in the Southern Ocean are available. These include: 1) SSH from the Ocean Surface Topography satellite missions (TOPEX/Poseidon, Jason-1, Jason-2, etc), 2) accurate geoids from satellite gravity missions (Gravity Recovery and Climate Experiment (GRACE) and the Gravity and Ocean Circulation Experiment (GOCE)), 3) T/S profiles and drift velocities from the Argo autonomous float program, and 4) full-depth, high-quality, CTD sections across the ACC at many longitudes (including Drake Passage, south of Africa, and south of Australia) from the World Ocean Circulation Experiment (WOCE) and more recently the CLIVAR Repeat Hydrography Program, some of them occupied repeatedly.

The following is a brief summary detailing the analysis we performed in order to use the WG80 method to estimate time-variable transport across the ACC, quantify its uncertainty, and examine whether it has significantly changed over the last decade.

In Chapter 2, we validated the method with available data. We used Argo, altimetry, and geoid data to estimate velocity in the upper 2000 dbar of the Southern Ocean [*Kosempa and Chambers*, 2014]. The zonal velocity (u) at each pressure level to 2000 dbar was determined by computing relative dynamic topography from Argo mapped T/S from each pressure level (e.g., 10 dbar, 20 dbar, 30 dbar, …, 2000 dbar) to surface. Relative dynamic topography was combined with absolute topography from altimetry and geoid to determine u at each level. Computed

velocity compared favorably with velocity estimated from Argo drift trajectories and that favorable validation enabled isolation of the ACC based on a defined persistence measure. Utilizing Jason-1 and Jason-2 altimetry and Argo observations, *Kosempa and Chambers* [2014] were able to generate a time series of ACC volume transport above 2000 dbar from 2005 to 2011. The chokepoints south of Africa (21°E meridian) and Tasmania (148°E meridian) were isolated as examples of the time variable transport that can be constructed from the velocity fields. The volume transport for each transect were evaluated.

By heavily relying on the sparse Argo array, the error associated in mapping temperature and salinity is a primary interest. In Chapter 3, we better quantified the mapping error estimated in Chapter 2. To quantify the impact of these errors on the estimation of upper-ocean transport, we conducted a sampling/mapping experiment using output from the high-resolution, eddy-resolving Southern Ocean State Estimation (SOSE) [*Mazloff et al.*, 2010]. We sampled the estimate at the times and locations of real-world SSH and Argo observations to generate a surrogate data set. These surrogate data were gridded and then integrated transports above 2000 dbar were subsequently computed. That transport was then compared to the original state estimate [*Kosempa and Chambers*, 2016].

It was found that the lower resolution of the raw Argo data causes higher mapping errors. We also assessed the effect of spatial averaging on the integrated transport, quantifying uncertainty in using the method to measure transport at a single transect. We analyzed repeat hydrographic sections across the ACC at several locations. Analysis of each transecct indicated areas most favorable to evaluating transport dynamics made available from altimetry and Argo. The transport time series from*Kosempa and Chambers* [2014] was subsequently been extended to 2014, and found no significant trend in zonal transport [*Kosempa and Chambers,* 2016].

Chapter 4 examines whether high-resolution gridded altimetry surface velocity products could improve transport estimates made along historical cruises that collected only subsurface temperature and salinity within the Antarctic Circumpolar Current (ACC) before 2005, when Argo data become available. We again designed experiments that rely upon output from the high-resolution Southern Ocean State Estimate (SOSE). We compared transect-sampled cumulative transports against the full-resolution state estimate cumulative transport. Three specific transect-sampled transports are investigated: 1) assuming a zero reference velocity at the deepest common level, 2) employing a pseudo-ADCP velocity at depth, and 3) utilizing a gridded pseudo-altimetric surface velocity. Using the results from these experiments, we quantified: 1) the ramifications of ignoring the reference velocity, 2) the uncertainty associated with sparse sampling during historical oceanographic cruises, and 3) differences when using a pseudo-altimetric surface velocity versus a pseudo-ADCP velocity at depth.

Chapter 5 synthesizes the results and points to future work that can strengthen this methodology for observing low frequency dynamics of the Southern Ocean.

CHAPTER 2:

Note to Reader

This chapter has been previously published in *Journal of Geophysical Research, Oceans*, 2014, 199(8), 4761-4776, and is included in Appendix A. Chapter 2 has been reproduced with permission from Wiley.

CHAPTER 3:

Note to Reader

This chapter has been previously published in *Journal of Geophysical Research, Oceans*, 2016, 121(11), 8063-8076, and is included in Appendix B. Chapter 3 has been reproduced with permission from Wiley.

CHAPTER 4:

The Antarctic Circumpolar Current (ACC) encircles the Antarctic continent unbounded on the eastern or the western sides. A lack of these boundaries results in significant currents extending deep into the water column because bathymetric boundary friction is insufficient to balance the work imparted by zonal winds. Currents at depth are required because accelerations from the surface winds balance with form drag created by bathymetry [*Munk and Palmen*, 1951; *Cunningham et al*, 2003]. The ACC's extension to depth poses unique observational challenges because determining the circumpolar transport requires more than temperature, salinity (TS) and pressure observations collected by ship casts or Argo floats. Transport estimates also require a measure of the velocity at the lowest common depth to reference the geostrophic shear obtained by temperature, salinity, and pressure observations.

An important source of TS observations is collection of subsurface data from ships. However, a reference velocity is not always collected during a ship cast. Computing a transport from velocity shear with a reference velocity assumed to be zero is the common observationalist definition of "baroclinic" transport and the one we use in this study. Depth-dependent, or "baroclinic" transports, have been computed from historical observations [e.g. *Rintoul and Sokolov*, 2001; *Legeais et al.*, 2005; *Swart et al.*, 2008]. Assuming a zero reference velocity is expected to bias the transport estimate and attenuate the variability [*Cunningham et al*, 2003]. The "barotropic" transport is commonly defined as the transport due to the true reference current, multiplied by the reference depth. The true transport is the sum of baroclinic and barotropic

contributions. An observed reference velocity estimates the additional component of the depth-independent, or "barotropic" transport when that reference velocity is spatially integrated across the full column. Combining TS observations with a coincident measurement of the reference current at depth obtained from shipboard lowered Acoustic Doppler Current Profilers (ADCPs) would, ideally, provide a suitable reference velocity [*Whitworth et al.,* 1982, *Heywood et al.,* 1999, *Donohue et al.,* 2001, *Cunningham et al*, 2003]. However, ADCP observations are not always collected during a ship's cruise [e.g. *Whitworth*, 1983; *Rintoul and Sokolov*, 2001; *Heywood and King*, 2002]. Additionally, ADCP collects the instantaneous true velocity, which even at great depths can contain small ageostrophic contributions (e.g. tides, internal waves).

Since 2004, Argo has been an important source of TS observations above 2000 dbar. Argo is particularly important in the collection of data in the Southern Ocean. Argo reduced the sampling bias toward the northern hemisphere by sharply increasing the number and coverage of temperature and salinity observations, regardless of the Austral season [*Roemmich and Gilson*, 2009]. While Argo does not directly observe velocity, velocity at a float's parking depth can be inferred from an individual float's position reporting [*Lebedev et al.,* 2007]. A previous study demonstrated this approach was inferior to using a surface reference velocity derived from satellite altimetry because of high levels of noise in the Argo drift currents and sparse sampling [*Kosempa and Chambers*, 2014]. Utilizing Jason-1 and Jason-2 altimetry and Argo observations, *Kosempa and Chambers* [2014] were able to generate a time series of ACC volume transport above 2000 dbar from 2005 to 2011. The time series has subsequently been extended to 2014 [*Kosempa and Chambers,* 2016]. Satellite altimeters have had nearly continuous coverage since late 1992, and could allow an extension of the transport time-series at some locations back to the early 1990s by incorporating TS data collected from ships that predate the Argo program.

Kosempa and Chambers [2016] investigated the uncertainty of gridding the sparse sampling of the Argo array in the Southern Ocean. Their focus was evaluating historical hydrographic cruise locations for potentially being combined with contemporary Argo products. That study found certain regions were less suitable for evaluating transport dynamics via the Argo array products [*Roemmich and Gilson*, 2009]. For example, the Drake Passage is too narrow and Argo too sparse for adequate sampling. The area near the Prime Meridian had significant autocorrelations in the error. The area near South Africa is dominated by high variability. *Kosempa and Chambers* [2016] found that the region south of Australia was optimal for observing transport dynamics from a combination of altimetry and Argo data. Specifically two separate transects -- south of west Australia and south of Tasmania -- displayed suitably low errors and had low in temporal autocorrelations.

This chapter examines whether gridded altimetry surface velocity products could improve transport estimates made along historical cruises that collected only subsurface temperature and salinity within the Antarctic Circumpolar Current (ACC). We designed analyses that rely upon output from the high-resolution Southern Ocean State Estimate (SOSE). Occupations of two transects are investigated. There are two occupations of a transect in the southern Indian basin and four occupations of the transect south of Tasmania. In the experiments, we compare transect-sampled cumulative transports against the full-resolution state estimate cumulative transport (the "truth"). Three specific transect-sampled transports are investigated: 1) assuming a zero reference velocity at the deepest common level, 2) employing a pseudo-ADCP velocity at depth, and 3) utilizing a gridded pseudo-altimetric surface velocity. Using the results from these experiments, we will quantify: 1) the ramifications of ignoring the reference velocity, 2) the uncertainty associated with sparse sampling during historical oceanographic cruises, and 3)

differences when using a pseudo-altimetric surface velocity versus a pseudo-ADCP velocity at depth.

4.1. Transects

Based on previous experiments of the method utilizing surface currents from altimetry to improve upper ocean transport [*Kosempa and Chambers,* 2016], historical ship cruises were identified for the Southern Ocean near 115°E and south of Tasmania from the CLIVAR and Carbon Hydrographic Data Office (CHDO) (http://cchdo.ucsd.edu/). CCHDO is a data repository for WOCE, CLIVAR and other oceanographic research programs. Locations and times of conductivity, temperature and depth (CTD) observations were downloaded in exchange format from http://cchdo.ucsd.edu/ for select occupations since TOPEX/Poseidon began collecting data in late 1992. We identified 2 occupations of a transect southeast of Australia (i08s_ct1 and i09s_09AR20041223_ct1, near 115°E) and 4 occupations of the transect south of Tasmania (sr03_b_ct1, sr03_c_ct1, sr03_ct1, 09AR20010104_ct1, near 148°E) (Table 4.1, Figure 4.1). Hereafter, these transects are referred to as "Australian" and "Tasmanian" for brevity. An algorithm was developed to remove instances of multiple casts at a given station. Because the SOSE model has a 1/6° grid size (section 2.2), we kept only the deepest cast in each 1/6° bin, with bins beginning at the first measurement. The ranges and numbers of casts for all occupations are listed in Table 4.1. Coverage of occupations are similar for the respective transects (Table 4.1). The Australian cruises were January of 1995 and December of 2004 into January of 2005. The Tasmanian occupations were March 1993, January 1994, January into February 1995 and January 2011. Tasmanian transects are split here into 'northern' and 'southern' limbs, as the northern limb runs roughly 18 degrees east of due North (Figure 4.1).

The southern limb runs roughly North/South. The Tasmanian transect is farther south than the Australian.

Table 4.1. Summary of cruise observations. Start and End times are written in decimal years.

Occupation	Designation	Southernmost Bound (°S)	Northernmost Bound (°S)	Number of Observations	Start	End
1	i08s_ct1	61.7583	36.2472	48	1995.00	1995.05
2	i09s_09AR20041223_ct1	61.7545	36.2685	44	2004.99	2005.03
1	sr03_b_ct1	64.9560	46.1578	41	1993.20	1993.24
2	sr03_c_ct1	64.9477	46.4093	41	1994.00	1994.04
3	sr03_ct1	64.9513	46.3949	38	1995.05	1995.08
4	09AR20010104_ct1	64.9405	46.4109	40	2011.01	2011.05

4.2. The Southern Ocean State Estimate and Sampling Transect Occupations

The Southern Ocean State Estimate (SOSE) is a general circulation model solution obtained from the MIT general circulation model (MITgcm) [http://mitgcm.org/]. SOSE assimilates available ocean observations using a least squares estimation technique, with a solution optimized by adjusting initial and boundary conditions acting as a control vector [*Wunsch and Heimbach*, 2007]. The estimate agrees with observations collected from several platforms and

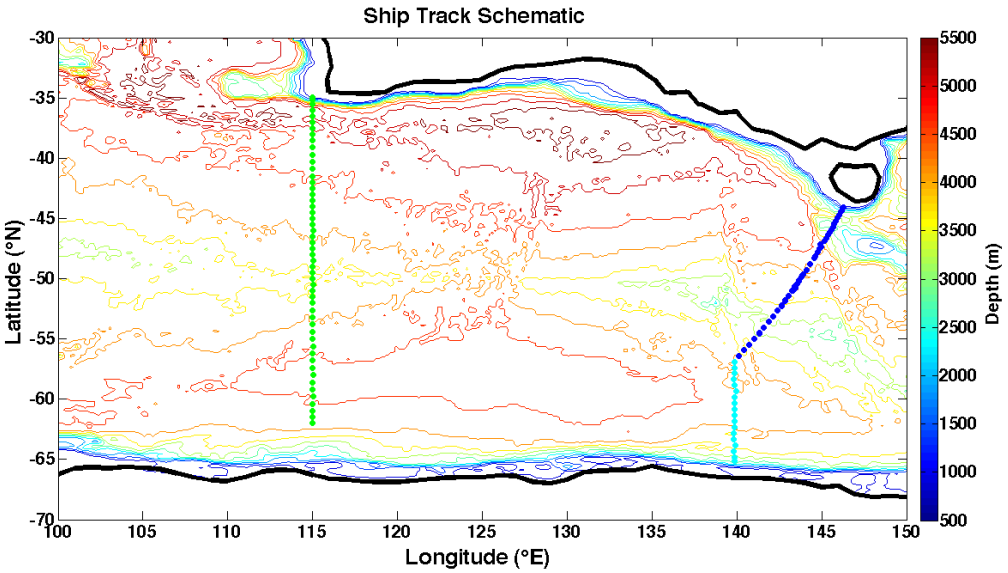

Figure 4,1. Locations of Transects. Australian (green) and Tasmanian south (cyan) and north (blue) limbs of transect observations for single, representative occupations. Depth obtained from Southern Ocean State Estimate (SOSE) is shown as colored contours.

produces a realistic mean zonal transport estimate [*Mazloff et al*., 2010]. Agreement with sea surface temperature observations and SOSE is with within expected uncertainty. However, SOSE is biased warm in the subtropics along with other local differences, for example eddy noise and frontal locations at ACC latitudes. The model is eddy permitting at 1/6° available at 5-day intervals from 2008 through 2010. SOSE's vertical grid cells spans the full column with 42 levels of varying thickness. The archived 'iteration 60' is used throughout this study [http://sose.ucsd.edu/sose_stateestimation_data_08.html].

We utilized SOSE outputs of temperature, salinity, hydrostatic pressure anomaly and absolute velocity components for this study. While the control experiment generates a synoptic sampling, the historical ocean-samplings were not synoptic, i.e. cruises were 1-2 weeks in duration. We were careful to replicate this quasi-synoptic sampling over time by using 'relative' times during each sampling of SOSE. Relative times were computed along each transect by subtracting the time of the first cast. The first SOSE-sampling period for each cruise was the earliest available SOSE products. We sampled the state estimate by isolating SOSE cells that surrounded the location of each cast for the full water column in SOSE. The isolated SOSE cells were then linearly interpolated to the relative times, locations, and depths of each observation in the cast, starting with the first available time-step in 2008. The depths were interpolated again to regular depth levels found in SOSE. One time step was then added for each subsequent SOSE-sampling step, and the process repeated until the end of the SOSE output in 2010. This procedure generated a total of 215 pseudo-occupations per cruise for the Australian transect and 210 for the Tasmanian transect. This was done in order to obtain sufficient samples to compute uncertainty statistics.

4.3. Experiments

The Australian control experiment computes transport directly from the SOSE velocity output at the full 1/6° resolution along a straight transect defined by the median longitude of all the occupations. The control experiment transects obtained are also synoptic, they all sample a single SOSE output date. The SOSE velocity product also includes ageostrophic velocity components in addition to the geostrophic velocities. The mean zonal velocities between two observation coordinates were vertically integrated above 3075 dbar (the deepest common level or 'reference depth'), and then spatially integrated from south to north across the median longitude of each respective cruise according to

$$T(y,t) = \int_{y_{south}}^{y_{north}} \int_{z_{reference}}^{z_{surface}=0} u(y,z,t)\, dz\, dy. \qquad (1)$$

Locations of observations in the north/south denoted y_{south} and y_{north} provide bounds of integration between adjacent casts. The integrated transport (T(y,t)) is then accumulated from the south across the entire transect for the cumulative transport to each value of *y*. For spatial coherency with the experimental variables in order to compare computed values, the high-resolution cumulative transport was interpolated to the latitudes found in each cruise.

Similar to the Australian transect, the Tasmanian south limbs of the control experiment samples SOSE zonal velocity at the full 1/6° resolution along a straight transect defined by the median longitude of each cruise. The latitude range found in Table 4.2 defines the northern limbs. The north limbs begin at the northernmost observation from the south limb. From that coordinate, a rhumb line (constant angle and distance) to the northernmost observation of each respective cruise was computed using http://geographiclib.sourceforge.net/cgi-

bin/RhumbSolveclear. SOSE zonal and meridional velocity outputs were interpolated to the center of each 1/6-degree line segment along each occupation's respective rhumb line. The meridional and zonal velocities were then used to estimate the velocity orthogonal to the rhumb line. The velocities for both the northern and southern limbs of the Tasmanian transects were spatially integrated to compute cumulative transport to each latitude (y) (Equation 1). Because the Tasmanian transect is in shallower water than the Australian (Figure 4.1), the deepest common level was 2575 dbar. The cumulative transports for this experiment is denoted $T_{control}$ throughout the paper.

Table 4.2. Tasmanian limb details. Latitudinal boundaries and deviation from north of the north limb of Tasmanian transect rhumb lines used for control experiment.

Occupation	Designation	North Limb Southernmost Observation (°S)	North Limb Northernmost Observation (°S)	Deviation from N (°)
1	sr03_b_ct1	56.6735	46.1578	17.50
2	sr03_c_ct1	56.6872	46.4093	17.48
3	sr03_ct1	56.5678	46.3949	17.50
4	09AR20010104_ct1	56.1798	46.4109	17.53

Subsequent experiments all rely on a relative dynamic ocean topography obtained from density computed from the sampled TS measurements, integrated from the deepest common level to each standard depth (z). The gradients of these relative dynamic topography data provide the relative geostrophic currents at depth. If the velocity at the deepest level is assumed to be zero, then these can be integrated to give the baroclinic transport as obtained by historical sampling, which is denoted here as T_{zero}. See *Kosempa and Chambers* [2014] for the details of the method.

The second sampling experiment assumes an ADCP velocity is available at the reference depth in order to additionally compute the total and barotropic component of geostrophic

transport as obtained by historical sampling. For the Australian and the south limbs of Tasmania, the SOSE zonal velocity at the reference depth was interpolated to the casts and is used to generate the pseudo-ADCP velocity. For the north limbs of the Tasmanian transect, the meridional and zonal velocities from SOSE at depth are converted into the orthogonal velocity. This pseudo-ADCP velocity was then multiplied by the depth and integrated to compute a barotropic transport, then added to T_{zero} to create a total geostrophic transport estimate that would be obtained from a hydrographic section with a lowered ADCP. The total geostrophic accumulated transport computed this way is designated T_{ADCP} throughout the paper.

The final sampling experiment assumes a gridded satellite altimeter product could provide a geostrophic velocity at the surface in which to reference the geostrophic shear [e.g., *Kosempa and Chambers,* 2014; 2016]. Gridded satellite altimeter products are available at the Copernicus Marine Environment Monitoring Service (CMEMS, now found at http://marine.copernicus.eu/services-portfolio/access-to-products/?option=com_csw&view=details&product_id=SEALEVEL_GLO_SLA_MAP_L4_REP_OBSERVATIONS_008_027, formerly available through AVISO). Near-global sea surface height anomalies relative to a 20-year climatology are available at daily resolution from 1993 and at 1/4° resolution. The time and grid information from CMEMS are used to manipulate SOSE estimates to produce pseudo-altimeter data.

To produce pseudo-altimeter products, the 1/6°, 5-day SOSE hydrostatic pressure anomaly outputs were first linearly interpolated to the 1-day resolution of the gridded altimeter products, and sea surface height was computed by dividing the hydrostatic pressure anomaly by acceleration due to gravity. The daily, 1/6° SOSE grids were then averaged over a 1/4° grid consistent with the altimetry product. The resulting products are pseudo-altimeter data. The

daily, 1/4° pseudo-altimeter grids were then spatially interpolated to the locations of each cast for each cruise, and the surface velocity orthogonal to the line segment defined by adjacent casts was obtained from the sea surface height gradient by assuming geostrophy [e.g. *Kosempa and Chambers*, 2014]. That surface velocity can be used as a reference for the velocity shear made available from the temperature and salinity fields to generate a velocity profile that includes both baroclinic and barotropic components [*Wunsch and Gaposchkin*, 1980; *Kosempa and Chambers*, 2014]. This velocity field was then spatially integrated to produce a cumulative transport to each latitude (Equation 1). This treatment of depth-integrated transport is denoted $T_{altimeter}$ throughout.

4.4. Results and Analysis Australia

Panels (a) and (c) in Figure 4.2 show the mean accumulated volume transport across the Australian transect for the different experimental treatments of transport. The temporal means of $T_{control}$, T_{zero}, T_{ADCP} and $T_{altimeter}$ are shown along with standard error (as error bars) for both occupations of the Australian transect from all samplings and accumulated to each latitude of the occupation. Standard error is the standard deviation divided by the square root of effective degrees of freedom. Effective degrees of freedom at each latitude were computed from lag-1 autocorrelation or decorrelation time where correlation goes below 0.5, whichever is smaller. This compared favorably with effective degrees of freedom computed from a non-parametric method [*Bendat and Piersol*, 1986]. The cumulative transports of both occupations are visually similar between the two occupations of the Australian transect.

Accumulating from 0 Sv at the extreme south, there is a steep increase from around 55°S until 45°S, indicating the strong current within core of the ACC. The maximum accumulated transport occurs to the north of this current core. Although the southern boundary (62.5°S) is just

out of coverage at this longitude, coverage does include the Southern Antarctic Circumpolar Front near 60.5°S [*Orsi et al.,* 1995]. The polar front occurs near 52.6S and Figures 4.2a and

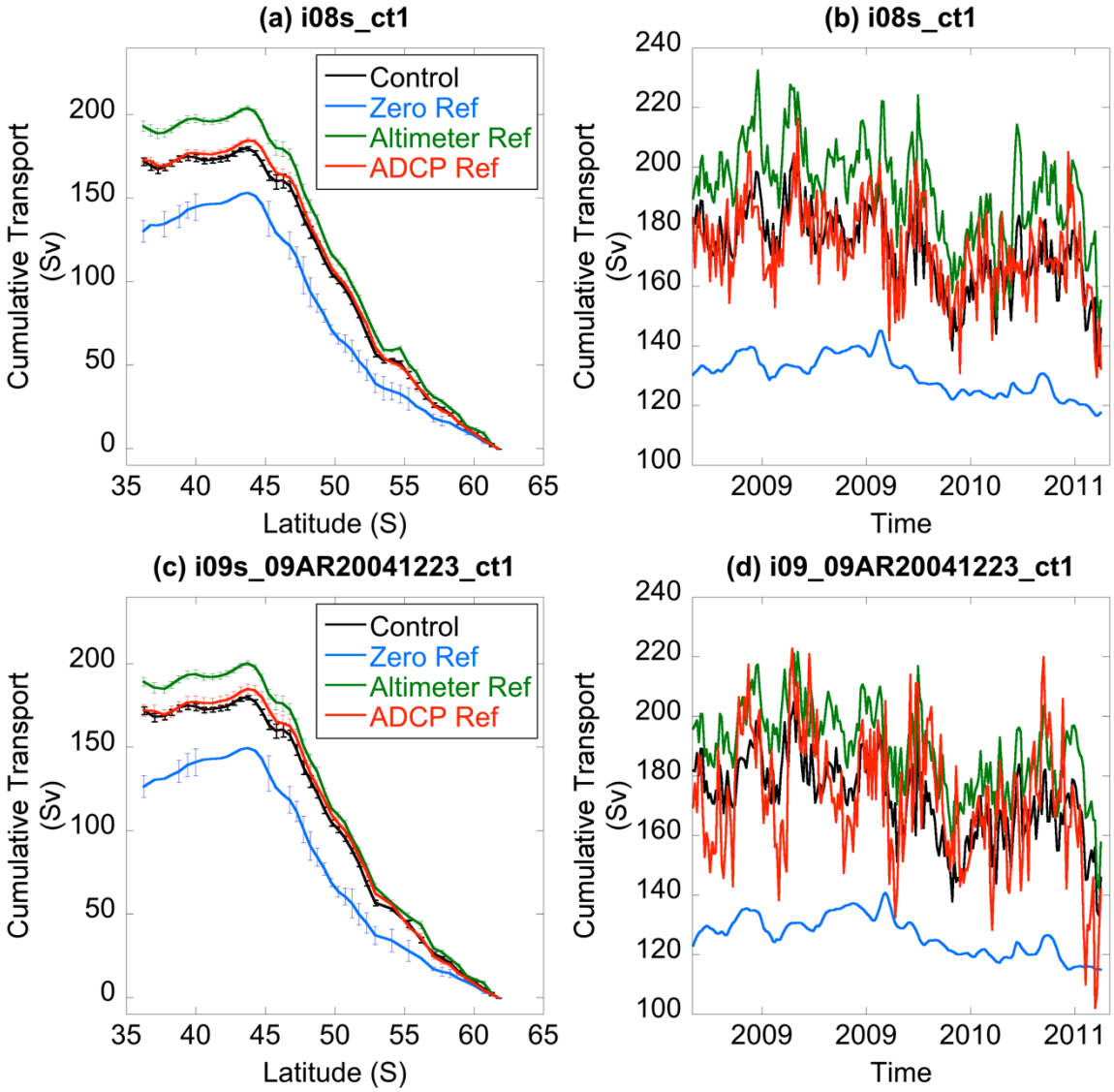

Figure 4.2. Cumulative transport and transport time series. (left panels) Mean cumulative integrated transport at the Australian transect for two cruises of $T_{control}$, T_{zero}, T_{ADCP}, $T_{altimeter}$. Error bars indicate standard error (one standard deviation divided by the square root of effective degrees of freedom). (right panels) Total transport time series accumulated over the entire cruise (exact bounds shown in Table 4.1) for two occupations at the Australian transect.

4.2c do show a sharp accumulation north of this latitude. Similar to the polar front, there is a moderation in accumulation while approaching the subantarctic front (49.4°S) from the south,

until the steep accumulation continues. Similar to the other fronts, there is decrease in accumulation while approaching the subtropical front near 40°S, again accumulating north of that latitude. Northward of that peak, a westward transport decreases the accumulated transport until 35°S.

$T_{control}$ has a consistent cumulative transport mean and standard deviation for the two samplings of the transect, as expected. T_{zero} consistently underestimates both the mean total transport, and the variability in comparison to $T_{control}$, being biased low by 42 to 46 Sv and with a standard deviation half that of $T_{control}$. Using a pseudo-ADCP velocity measurement results in no significant bias in transport, but slightly higher standard deviations (Table 4.3).

Table 4.3. Summary statistics for cumulative transports. Statistics are quoted for time series across full integration bounds (Table 4.1).

Occupation	Designation	Transport Treatment	Correlation with Tcontrol	Mean (Sv)	Standard Deviation (Sv)	Variance Explained (%)
1	i08s_ct1	control	1.00	172	14	NA
2	i09s_09AR20041223_	control	1.00	172	14	NA
1	i08s_ct1	zero	0.69	130	7	43
2	i09s_09AR20041223_	zero	0.65	126	7	39
1	i08s_ct1	ADCP	0.69	173	15	32
2	i09s_09AR20041223_	ADCP	0.57	172	22	-74
1	i08s_ct1	Altimeter	0.92	193	16	78
2	i09s_09AR20041223_	Altimeter	0.97	189	14	93
1	sr03_b_ct1	control	1.00	181	10	NA
2	sr03_c_ct1	control	1.00	182	10	NA
3	sr03_ct1	control	1.00	182	10	NA
4	09AR20010104_ct1	conrol	1.00	182	10	NA
1	sr03_b_ct1	zero	0.80	131	8	64
2	sr03_c_ct1	zero	0.81	132	8	66
3	sr03_ct1	zero	0.74	132	8	55
4	09AR20010104_ct1	zero	0.75	128	10	51
1	sr03_b_ct1	ADCP	0.73	188	12	30
2	sr03_c_ct1	ADCP	0.77	191	13	26
3	sr03_ct1	ADCP	0.65	191	15	-26
4	09AR20010104_ct1	ADCP	0.70	179	14	0
1	sr03_b_ct1	Altimeter	0.71	203	13	19
2	sr03_c_ct1	Altimeter	0.81	202	13	44
3	sr03_ct1	Altimeter	0.80	201	15	21
4	09AR20010104_ct1	Altimeter	0.66	194	14	-19

Using pseudo-altimeter surface velocities results in a transport that is biased high by 17 to 21 Sv, but comparable standard deviation (Table 4.3). All statistics quoted refer to the accumulated transport between southern and northern bounds in Table 4.1, unless otherwise specified. Mean and standard deviations when transport is accumulated to only 40.5931°S (first cruise) and 40.5880°S (second cruise) are given in Table 4.4.

We also examined a time-series of transport integrated across the full integration bounds (Table 4.1) based on sampling the SOSE model along the transect (Figures 4.2b and 4.2d). This time series shows the biases in T_{zero} and $T_{altimeter}$, as well as the differences and similarity in standard deviation. The percentage of $T_{control}$ variance explained by T_{zero} is 43% and 39% for the two occupations, indicating that the dynamics of the control experiment are only weakly represented by just the baroclinic component along the Australian transect. Alternatively, T_{ADCP} weakly represents the variance well during the better-sampled first cruise (explaining 32%) but adds signal and noise due to the sampling of the second cruise causing a negative variance explained (-74%). $T_{altimeter}$, although biased, explains 79 and 93% of the variance in the control for the first and second cruise respectively, outperforming both T_{zero} and T_{ADCP} in terms of recovering the variability.

The Australian time series differences are not just due to high-frequency (sub-monthly) variability. After applying a 25-day boxcar filter (Figure 4.3a, 4.3b), there are still substantial differences in the baroclinic-only calculation (T_{zero}) and the calculations including a barotropic estimate ($T_{control}$, T_{ADCP}, $T_{altimeter}$). The barotropic variability at the Australian transect is high because the Australian-Antarctic abyssal plain is characterized by closed f/H contours (H represents depth), reducing the constraints imposed by potential vorticity. Free from constraints imposed by bathymetric gradients, regions of closed f/H contours display elevated barotropic

variability. The dominance of the barotropic mode at this location and timescale is explored in *Weijer et al.* [2009] and *Weijer* [2010].

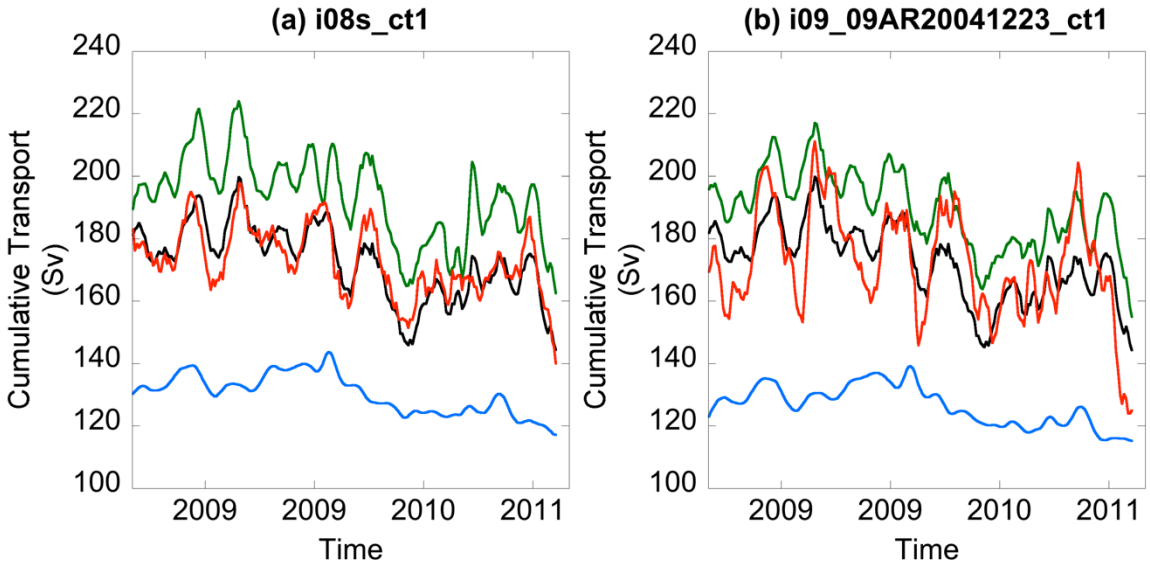

Figure 4.3. Transports with 25-day boxcar low pass filter. Shown for both occupations of Australian.

We quantified the error that each experiment has in reproducing the control transport variability by examining the standard deviation of the residuals of the time-series (i.e., $T_{zero} - T_{control}$, $T_{ADCP} - T_{control}$, $T_{altimeter} - T_{control}$). Here, the error is taken as the standard deviation of the residuals for the time-series integrated to the northernmost latitude. The error in T_{zero} is 10 Sv and 11 Sv for the first and second occupations, respectively. The errors in T_{ADCP} differ depending on the cast sampling, being 11 Sv for the first sampling and 18 Sv for the second sample. For $T_{altimeter}$, the error is 6 and 4 Sv for the first and second cruises respectively. Thus, although using altimetric surface velocity will probably lead to a biased transport, the variability of the transport is better represented than using sampled velocities at depth. This phenomenon is evident in the higher correlations between $T_{control}$ and $T_{altimeter}$ time series (Table 4.3).

4.5. Results and Analysis Tasmania

The temporal means of $T_{control}$, T_{zero}, T_{ADCP} and $T_{altimeter}$ are shown with error bars of standard error for the 4 occupations of the Tasmanian transect (Figures 4.4). Values are shown for the accumulation of transport across all observations (the entire range of coverage unless otherwise specified, starting with 0 Sv a the far south, Table 4.1) and statistics are shown in Table 4.3.

Similar to panels (a) and (c) of Figure 4.2, panels (a), (c), (e), (g) of Figure 4.4 show the mean accumulation of volume transport that traverses the transect. Error bars indicate the standard error, computed similarly as the Australian transect. The accumulation patterns for the Tasmanian transect are similar to the Australian transect, although narrower and shifted southward. Starting from 0 Sv at the extreme south, there is a steady build in accumulated transport until 56°S, indicating an eastward current at those latitudes. A return westward current is inferred from the decrease in accumulated transport from 56°S until 53°S, before a sharp increase in accumulated transport from 53°S until 50°S. This sharp increase indicates the strong eastward current of the core of the ACC. Having more southerly sampling, the Tasmanian transect does extend south to the southern boundary (64°S), which is very close to the Southern Antarctic Circumpolar Front (-63.7°S) at this longitude [*Orsi et al.*, 1995]. A local peak occurs just south of the Polar Front at 55.7°S, before declining until just south of the Subantarctic Front (51.9°S). Accumulation occurs north of the Subantarctic Front until a brief plateau near 48°S. The accumulation pattern occurs again near the Subtropical Front, where transport peaks just south of 46.9°S. Statistics for the accumulation to 47°S are given in Table 4.4.

There are subtle but important differences in the occupations. The first, second, and third occupation are similar, contrasting the more unique fourth occupation. The first occupation (Figure 4.4a) shows T_{ADCP} mirroring $T_{control}$, except near 47°S. $T_{altimeter}$, alternatively, fails much

further south by overestimation near both 60°S and 52°S. This pattern of success and failure is similar to Figures 4.4a, 4.4c, and 4.4e. The results of the unique sampling of the final occupation of the Tasmanian transect is visible in Figure 4.4g. There is an instance of increased accumulated transport in $T_{control}$ that is not found in the sampled products occurring at 57°S. Similarly, near 50°S, $T_{control}$ indicates a gradient not captured by either T_{ADCP} or $T_{altimeter}$.

T_{zero} underestimates the accumulated transport at Tasmania with biases consistently near 50 Sv. However, unlike the Australian transect, the standard deviations are in much better agreement for $T_{control}$. Also similar to the Australian transect, T_{ADCP} is shown to have the least amount of bias relative the other two treatments of sampled transport. Similarly, $T_{altimeter}$ shows high bias while also inflating the variability. The biases of $T_{altimeter}$ are similar for the first three cruises (22, 20, 19 Sv) while differing on the fourth (12 Sv). These changes in biases present a problem if one wants to combine discrete observations using $T_{altimeter}$ to infer changes in transport over the 1990s.

T_{zero} better explains more of the variability and more consistently (64, 66, 55, 51% of variance explained) than the other transport experiments. T_{ADCP} struggles to represent the variability (30, 26, -26, 0% variance explained) as does $T_{atimeter}$ (19, 44, 21, -19% of variance explained). The correlations are consistent for all treatments of transport and the variability is best represented by T_{zero}, having been overestimated by both T_{ADCP} and $T_{altimeter}$.

The peak in cumulative Tasmanian transport for the 4 occupations occurs near 47°S and a region of little accumulated transport with high standard error to the immediate south of that peak. Each of the transport experiments has difficulty in reproducing the variability associated with this area of high standard error (Table 4.4). Each treatment has the variability explained significantly reduced. However, T_{zero} is the only treatment to explain some variance by

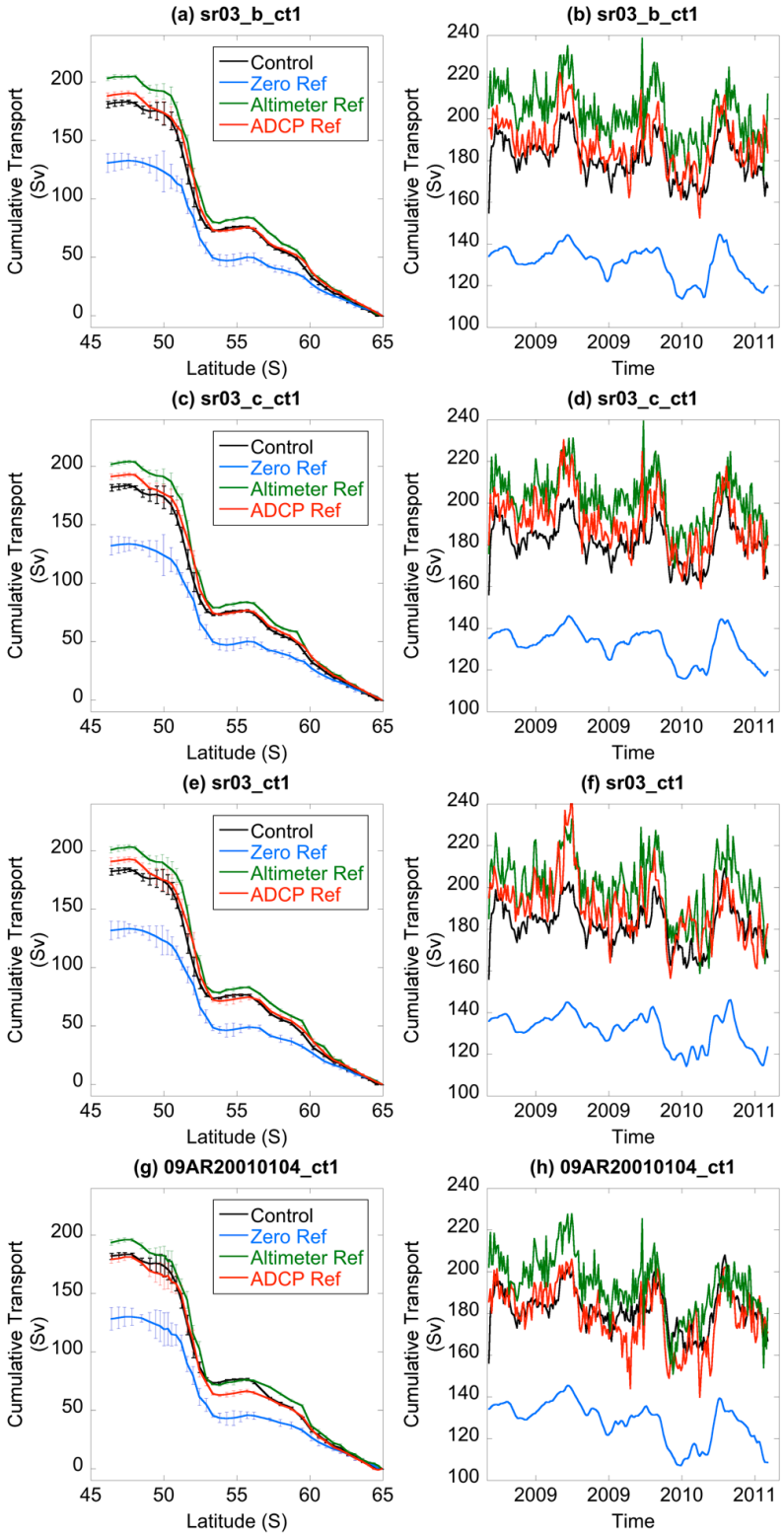

Figure 4.4. (left panels) Tasmanian mean cumulative integrated transports. (right panels) Total cumulative transport time series for each treatment of transport for each occupation.

remaining a positive quantity, however small. The final occupation of the Tasmanian transect does indicate a negative variance explained for T_{zero}. The statistics near the area of high standard error are negatively affected, indicating the full transect transport is more effective in estimating transport dynamics.

Table 4.4. Summary statistics for reduced integration bounds. Bounds are integrated to 40°S for Australian and 47°S for the Tasmanian transects.

Occupation	Designation	Transport Treatment	Mean (Sv)	Standard Deviation (Sv)	Variance Explained (%)
1	i08s_ct1	control	172	12	NA
2	i09s_09AR20041223_ct1	control	172	12	NA
1	i08s_ct1	zero	146	7	20
2	i09s_09AR20041223_ct1	zero	142	8	17
1	i08s_ct1	ADCP	176	13	5
2	i09s_09AR20041223_ct1	ADCP	176	21	-1
1	i08s_ct1	Altimeter	196	16	92
2	i09s_09AR20041223_ct1	Altimeter	192	14	93
1	sr03_b_ct1	control	183	8	NA
2	sr03_c_ct1	control	183	7	NA
3	sr03_ct1	control	184	7	NA
4	09AR20010104_ct1	conrol	183	8	NA
1	sr03_b_ct1	zero	133	6	24
2	sr03_c_ct1	zero	133	6	28
3	sr03_ct1	zero	133	6	16
4	09AR20010104_ct1	zero	130	7	-29
1	sr03_b_ct1	ADCP	190	11	-62
2	sr03_c_ct1	ADCP	193	11	-42
3	sr03_ct1	ADCP	193	12	-108
4	09AR20010104_ct1	ADCP	181	11	-132
1	sr03_b_ct1	Altimeter	205	11	-46
2	sr03_c_ct1	Altimeter	204	11	-9
3	sr03_ct1	Altimeter	203	12	-56
4	09AR20010104_ct1	Altimeter	196	11	-99

4.6. Discussion:

Kosempa and Chambers [2014] assumed purely random errors in the validation against Argo float trajectories. *Kosempa and Chambers* [2016] better quantified errors than *Kosempa and Chambers* [2014] by investigating systematic errors that arise from mapping sampled data.

Kosempa and Chambers [2016] showed the error in the deep current estimated from a combination of altimetry and Argo data is anticorrelated with the error in depth-dependent currents estimated from only Argo. The negative correlation in error is now seen in hydrographic sections obtained from ships, as this negative correlation again manifests in the hydrographic sections. Anticorrelation of errors is attributed to attenuation of the reference velocity signal and also attenuation of the velocity shear throughout the water column.

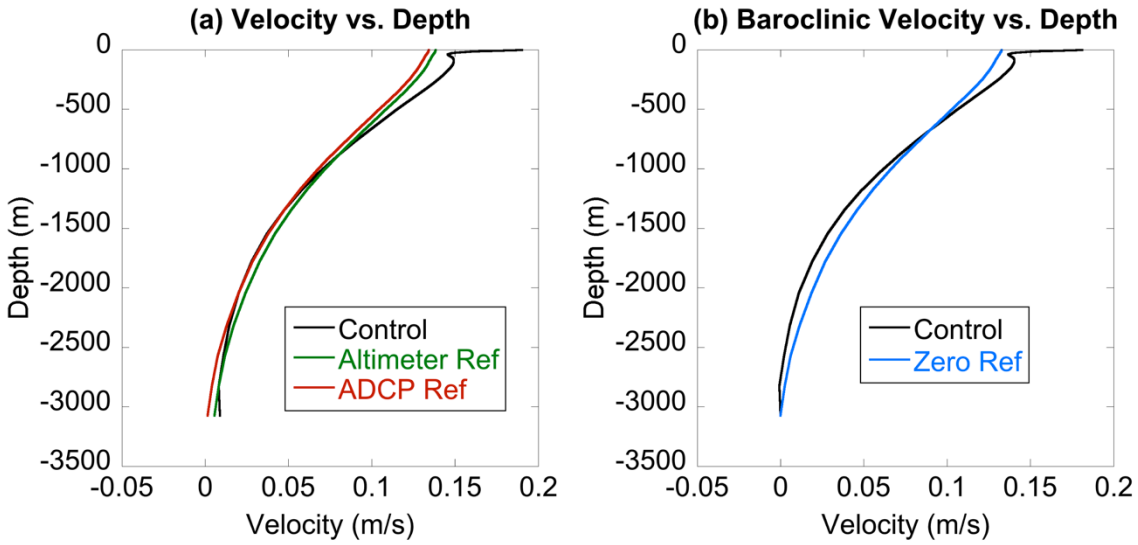

Figure 4.5. (a) Three treatments of velocity versus depth. Treatments are Control, altimeter-referenced, and ADCP-referenced. (b) Baroclinic contribution of control velocity and zero reference velocity versus depth. The profile is representative of results (shown for 49.2°S at the first Australian occupation i08s_ct1).

Each of our results show $T_{altimeter}$ biased high relative to $T_{control}$. This high bias is counterintuitive because the processing of dynamic ocean topography (specifically, averaging

from SOSE to pseudo altimeter products) is expected to attenuate the gradient of sea surface height (i.e. surface velocity). Similarly, the gradient of sea surface height between two locations computes the mean velocity between those locations, which would not result in high bias. The high bias in $T_{altimeter}$, therefore, is not because the surface velocity estimated by the altimeter is biased high. The same line of reasoning can be applied to the averaging of ADCP measurements between hydrographic station pairs. Representative profiles for the control, altimeter-referenced and ADCP-referenced velocities are shown from the first occupation of the Australian transect (Figure 4.5a). Figure 4.5a shows the altimeter-referenced velocity profile to be biased *low* near the surface and shows ADCP-referenced velocity to be biased *low* at the reference depth (note the ageostrophic contribution to the control velocity nearest the surface contaminates the comparison). This low bias of each reference velocity is intuitive. The underestimation of reference velocity is not manifested in the results because the velocity shear is likewise attenuated (Figure 4.5b). Figure 4.5b shows the same representative velocity from the control experiment now with the reference depth velocity removed from the entire column (what we have defined as the baroclinic contribution). Similarly, the altimeter and ADCP referenced velocity profiles are shown with their deepest velocity removed. Since they are identical, Figure 4.5b identifies them as the zero reference velocity profile, synonymous with velocity shear. The attenuation of velocity shear, or the 'straightening' of the shear profile (Figure 4.5b), shows the historical hydrographic sampling of TS struggling to represent the finer structure of the velocity profile. Figure 4.5b shows the bias resulting from this attenuation is depth dependent. Figure 4.5b indicates T_{zero} would underestimate baroclinic transport above 600 m and overestimate baroclinic transport below 600 m at this representative location. This attenuation of velocity shear resulting from ship sampling emerges in our results as high bias in $T_{altimeter}$ relative to

$T_{control}$. Similarly, T_{ADCP} has no bias relative to $T_{control}$ fortuitously, given the depth-dependent nature of shear attenuation (Figure 4.5b). This analysis shows the correlation in errors to be dependent on the chosen reference depth. In the representative case of Figure 4.5, errors are positively correlated above approximately 600 m, and negatively correlated below 600 m. Combining the deep current and baroclinic currents over the full column then results in a lower total transport error than considering the depth-independent and -dependent transport errors separately.

While Figures 4.2 and 4.4 show T_{zero} to underestimate $T_{control}$, T_{zero} overestimates the baroclinic contribution to $T_{control}$ simply because of our choice of reference depth. Similarly, the barotropic contributions of $T_{altimeter}$ and T_{ADCP} underestimate the barotropic contributions to $T_{control}$.

The results show the choice of reference velocity leads to errors that are transect and occupation specific. T_{zero} has error of 11 Sv for both occupations of the Australian transect and a significant bias (-42 and -46 Sv), both of which are larger than for $T_{altimetry}$. However, that error for T_{zero} drops to 7 Sv for each occupation of the Tasmanian transect, less error than both T_{ADCP} and $T_{altimeter}$ at the Tasmanian transect, although there is still a large bias (-50, -50, -51, -53 Sv). The value of the bias for Tzero is more consistent than for $T_{altimetry}$.

The explanation for these differences can be deduced from the time series of cumulative transport (e.g. Figures 4.2b vs. 4.4b). The baroclinic transport (T_{zero}) does not fully represent the variable total transport at the Australian transect for periods longer then a month, but it does at the Tasmanian transect. Using a pseudo-altimetry velocities as a reference velocity or even a pseudo-ADCP adds significant noise compared to just assuming a zero velocity for the

Tasmanian transect. However, ignoring the reference velocity does significant bias the mean transport for both transects.

The high error of T_{ADCP} shown as the standard deviation of residuals during the 2nd cruise along the Australian transect showcases a different phenomenon. T_{ADCP} is shown to be highly variable during the second cruise, however, the bias of the second cruise is unaffected. This is due to a decrease of 4 casts from cruise 1 to cruise 2 (Table 4.1). Under sampling by 4 ship casts is enough to significantly add noise to the transport calculation when sampling the relatively narrow jets that comprise the Antarctic Circumpolar Current. That under sampling problem is compounded by the fact that the suboptimal velocity is applied to ever-larger areas when spatially integrating the velocity field to produce a volume transport. This under sampling is less of an issue with altimeter measurements because they inherently average more over space and time, and more consistently. Considering we have not included errors from removing ageostrophic contributions from true instantaneous velocities, these results suggests little advantage in using ADCP in lieu of altimetric surface velocities simply based on sampling, should ADCP observations exist. A comparison of ADCP and altimetric reference velocities, including instrumental errors, could be warranted at locations that did collect ADCP measurements. This line of experimentation is left for future work.

Results suggest that using surface altimetry along the Australian transect would better represent total transport, albeit biased high. For the Tasmanian transect, however, using a reference velocity of zero best represent the variable transport, despite a low, but nearly constant bias. Considering that we have not included errors from altimetry or the mean geoid, these results suggest serious difficulties in trying to combine transport estimates from altimetry and hydrographic section data in the 1990s with altimetry and Argo data from 2005 onwards.

Although these difficulties are less severe for the Australian transect, it has only one occupation prior to Argo. While the Tasmanian transect has more occupations prior to Argo, these results indicate there is no benefit of using surface currents from altimetry as a reference velocity over a zero velocity at depth.

CHAPTER 5:

This work presents a foundation for empirical observation of the total geostrophic transport in the World Ocean. The work described herein is not a standard methodology but a first comprehensive attempt at validation and quantitative evaluation of a nascent method. We succeeded in validating WG80 as a method and quantifying errors in the observational sampling. Analysis indicates WG80 is approaching the ability to investigate subsurface transport dynamics and how those dynamics respond to low frequency climate dynamics. The standardization of methodology and quality procedures will be a sophisticated undertaking. Consolation can be found in the continued collection and refinement of observational capabilities.

Kosempa and Chambers [2014] validated basin-wide subsurface currents against estimates derived from the drift of Argo floats [*Lebedev et al.,* 2007]. The computed currents compared favorably to estimated currents at 1000 dbar based on Argo float trajectories. The mean transports from a combination of altimetry and Argo T/S between Africa and Tasmania data were also close to values of ACC depth-dependent transport of ~147 Sv [*Rintoul and Sokolov*, 2001. The standard deviation between 5-year mean velocities at 1000 dbar from our estimate and those from Argo trajectories was only slightly larger than the sampling error estimated for the drift calculation, verifying the validation. However, *Kosempa and Chambers* [2014] assumed purely random errors in the validation against Argo float trajectories, while *Kosempa and Chambers* [2016] investigated systematic errors that arise from mapping sampled data. *Kosempa and Chambers* [2016] showed the error in the deep current estimated from a

combination of altimetry and Argo data is anticorrelated with the error in depth-dependent currents estimated from only Argo. The significant correlation in error is seen in both the Argo and hydrographic sections obtained from ships, as this negative correlation again manifests in the hydrographic sections found in Chapter 4. Anticorrelation of errors is attributed to attenuation of the reference velocity signal and also attenuation of the velocity shear throughout the water column. Observed reference velocities were shown to underestimate the true velocity because of attenuation. Hydrographic sections, alternatively, attenuate the velocity shear, which over- or under-estimate the velocity depending on the depth level (Figure 4.5). The analysis of Chapter 4 shows the correlation in errors to be dependent on the chosen reference depth. In the representative case of Figure 4.5, errors are positively correlated above approximately 600 m, and negatively correlated below 600 m. Combining the deep current and baroclinic currents over the full column then results in a lower total transport error than considering the depth-independent and/or -dependent transport errors separately. The work of *Kosempa and Chambers* [2016] also investigated the errors as a function of geography by showing the correlation of errors and the error itself to be geographically dependent. Analysis of regional mapping error points to areas that are better suited for using WG80 to analyze transport dynamics than others, with the areas south of Australia displaying optimal errors. The investigation of these transects by ship sampling shows the choice of reference velocity to manifest errors that are transect and occupation specific, which complicates improvement of transport estimates from temperature and salinity observations alone. Using a pseudo-altimetry velocities as a reference velocity or even a pseudo-ADCP adds significant noise compared to just assuming a zero velocity for the Tasmanian transect. Results suggest that using surface altimetry along the Australian transect would better represent total transport, albeit biased high. For the Tasmanian transect, however,

using a reference velocity of zero best represent the variable transport, despite a low, but nearly constant bias. While the Tasmanian transect has more occupations prior to Argo, these results indicate there is no benefit of using surface currents from altimetry as a reference velocity over a zero velocity at depth. The errors and biases of ADCP- and altimetry-referenced transport estimates were too variable to justify adding real-world estimates to the Argo time series.

Kosempa and Chambers [2014] was unable to reproduce the mean or variable transport across a single transect with any accuracy (their Table 2, Figure 10). Although conservation of mass was unrealistic, analysis showed the error can be reduced by >70% by averaging the gridded results over a wider zonal area, thereby increasing the confidence in both mean and time variable transport. Extending this technique, ACC transport averaged over the entire Indian basin (21°E – 148°E) was significantly correlated with the Antarctic Oscillation at low frequencies, consistent with correlations seen in the GRACE data [*Bergmann and Dobslaw*, 2012; *Makowski et al*., 2015] and bottom pressure and sea level data in the Drake Passage [*Meredith et al*., 2004]. The transport time-series of *Kosempa and Chambers* [2016] captured much of the interannual SAM variability after 2006, but there is a substantial difference in 2008 and 2009, when the estimated transport anomaly is zero or negative but the SAM is positive (their Figure 10b). No signs of this error are apparent in the residual analysis. This suggested that by averaging over an entire basin, one can compute realistic time-variable zonal transport with this method but significant work on spatial averaging and isolation of the ACC is required to explain the discrepancy in the SAM time series from *Kosempa and Chambers* [2016].

Kosempa and Chambers [2014] did not find any significant trend in zonal transport above 2000 dbar in roughly the same region of the south Indian Ocean where *Makowski et al*. [2015] found a strong trend in GRACE-derived transport. Furthermore, the change in spatial

averaging and investigation in a different geographic area presented a less convincing SAM tracking in *Kosempa and Chambers* [2016]. *Kosempa and Chambers* [2016] found no trend in zonal transport, but did find positive trends in the depth independent transport and negative trends in the depth dependent transport. Although this trend pattern could be interpreted as consistent with eddy saturation, caution should be exercised, given the less favorable agreement with the SAM.

Kosempa and Chambers [2016] demonstrated that the barotropic variability (i.e., the component due to the reference velocity at depth) is the dominant source of variability, explaining well over 85% of the low-frequency variance that is most correlated with SAM. Using only the density information and assuming a zero velocity at depth (as is typically done with hydrographic sections) would have severely underestimated the transport variability. Thus, understanding and measuring the currents at the deepest common level is critical to measuring the full geostrophic transport variability.

Future work needs to investigate the sensitivity of spatial isolation of the ACC. We attribute inconsistent results to inadequate isolation of the ACC using the persistence measure, incomplete data coverage to the extreme south, contribution of signal from the subtropical front to the north, or failure to cover the full chokepoint width.

Perhaps the most significant failure is ignoring the meridional transport component. All of the transport considered herein is purely zonal and the ACC has significant departures from purely zonal flow. The total transport (which includes the meridional contribution to transport), therefore, must be included in future work.

Kosempa and Chambers [2014] used coincident mapped T/S profiles from Argo and coherent mapping functions for all data sets to reduce problems of using different resolutions.

However, Argo data have been mapped with a global covariance function that also includes longer-scale correlations from the tropics. Method improvement includes investigation of the covariance function of multiple variables in the Southern Ocean. The covariance function should be computed for different levels, as the upper ocean temperature and salinity likely have different decorrelation scales than those for the deeper ocean. The covariance function used in the optimal interpolation procedure is based on a worldwide autocovariance obtained from altimetry and a reanalysis should better reflect the covariance structure of the ACC.

The relatively short instrument record creates the problem of a well-defined climatology, which is crucial for the optimal interpolation and is known to be a concern for the mapping of Argo data in this region [*Roemmich and Gilson*, 2009]. With continued Argo observations in the Southern Ocean, this will become less of a problem. A longer instrument record will not only help the climatology but also increase confidence in our trend and correlation analyses. In addition to the weak climatology, there are only 4 cycles of the SAM during the Argo period, and the time series of *Kosempa and Chambers* [2016] was noticeably disparate from the SAM relative to *Kosempa and Chambers* [2014].

Future work can now optimize the methods described with confidence in the ability to estimate currents of the World Ocean to improve our understanding of low-frequency transport of the ACC and the contribution of subsurface currents to that variability.

REFERENCES

Bendat J., Piersol, A., (1986). Random Data: Analysis and Measurement Procedure, 2nd Edition, Revised and Expanded. John Wiley and Sons, 96.

Bergmann, I., and H. Dobslaw (2012), Short-term transport variability of the Antarctic Circumpolar Current from satellite gravity observations, *J. Geophys. Res., 117*, C05044, doi:10.1029/2012JC007872.

Cunningham, S. A., S. G. Alderson, B. A. King, and M. A. Brandon (2003), Transport and variability of the Antarctic Circumpolar Current in Drake Passage. Journal of Geophysical Research, 108(C5), 8084, doi: 10.1029/2001JC001147.

Donohue, K., E. Firing, and S. Chen (2001), Absolute Geostrophic Velocity within the Subantarctic Front in the Pacific Ocean. International WOCE Newsletter, Number 36, 12.

Farneti, R., T. Delworth, A. Rosati, S. Griffies, and F. Zeng, (2010). The Role of Mesoscale Eddies in the Rectification of the Southern Ocean Response to Climate Change. *J. Phys. Oceanogr.,* **40**, 1539–1557, doi: 10.1175/2010JPO4353.1.

Fyfe, J. C., and O. A. Saenko (2006), Simulated changes in the extratropical Southern Hemisphere winds and currents. Geophysical Research Letters, 33(L06701), doi: 10.1029/2005GL025332.

Gnanadesikan, A., and R. W. Hallberg, (2000), On the Relationship of the Circumpolar Current to Southern Hemisphere Winds in Coarse-Resolution Ocean Models. *J. Phys. Oceanogr.*, **30**, 2013–2034.
doi: http://dx.doi.org/10.1175/1520-0485(2000)030<2013:OTROTC>2.0.CO;2

Hallberg, R., and A. Gnanadesikan (2006), The Role of Eddies in Determining the Structure and Response of the Wind-Driven Southern Hemisphere Overturning: Results from the modeling Eddies in the Southern Ocean (MESO) Project. *Journal of Physical Oceanography, 36*, 2233.

Heywood, K. J., Sparrow, M. D., Brown, J., & Dickson, R. R. (1999). Frontal structure and Antarctic bottom water flow through the Princess Elizabeth Trough, Antarctica. Deep Sea Research Part I: Oceanographic Research Papers, 46(7), 1181-1200.

Heywood, K. J., & King, B. A. (2002). Water masses and baroclinic transports in the South Atlantic and Southern oceans. Journal of Marine Research, 60(5), 639-676.

Knudsen, P., R. Bingham, O. Andersen, M. Rio (2011), A global mean dynamic topography and ocean circulation estimation using a preliminary GOCE gravity model, Journal of Geodesy, doi: 10.1007/s00190-011-0485-8.

Kosempa, M., and D. P. Chambers (2014), Southern Ocean velocity and geostrophic transport fields estimated by combining Jason altimetry and Argo data, J. Geophys. Res. Oceans, 119, 4761–4776, doi:10.1002/2014JC009853.

Kosempa, M., and D. P. Chambers (2016), Mapping error in Southern Ocean transport computed from satellite altimetry and argo, J. Geophys. Res. Oceans, 121, doi:10.1002/2016JC011956.

Langlais C. E., S. R. Rintoul, and J. D. Zika, (2015), Sensitivity of Antarctic Circumpolar Current Transport and Eddy Activity to Wind Patterns in the Southern Ocean. *J. Phys. Oceanogr.*, 45, 1051–1067.
doi: http://dx.doi.org/10.1175/JPO-D-14-0053.1

Lebedev, K. V., H. Yoshinari, N. A. Maximenko, and P. W. Hacker (2007), YoMaHa '07:Velocity data assessed from trajectories of Argo floats at parking level and at the sea surface. IPRC Technical Note, 4(2).

Legeais, J. F., Speich, S., Arhan, M., Ansorge, I., Fahrbach, E., Garzoli, S., & Klepikov, A. (2005). The baroclinic transport of the Antarctic Circumpolar Current south of Africa. Geophysical Research Letters, 32(24).

Makowski, J. K., Chambers, D. P., and Bonin, J. A. (2015). Using ocean bottom pressure from the Gravity Recovery and Climate Experiment (GRACE) to estimate transport variability in the southern Indian Ocean. Journal of Geophysical Research: Oceans.

Mazloff, Matthew R., Patrick Heimbach, Carl Wunsch, 2010: An Eddy-Permitting Southern Ocean State Estimate. *J. Phys. Oceanogr.*, **40**, 880–899.
doi: http://dx.doi.org/10.1175/2009JPO4236.1

Meredith, M. P., P. L. Woodworth, C. W. Hughes, and V. Stepanov (2004), Changes in the ocean transport through Drake Passage during the 1980s and 1990s, forced by changes in the Southern Annular Mode, *Geophys. Res. Lett., 31*, L21305, doi:10.1029/2004GL021169.

Meredith, M. P., A. C. Naveira Garabato, A. McC. Hogg, and R. Farneti, (2012) Sensitivity of the Overturning Circulation in the Southern Ocean to Decadal Changes in Wind Forcing. *J. Climate*, **25**, 99–110.
doi: http://dx.doi.org/10.1175/2011JCLI4204.1

Morrison, A. K., and A. McC. Hogg, (2013) On the Relationship between Southern Ocean Overturning and ACC Transport. *J. Phys. Oceanogr.*, **43**, 140–148.
doi: http://dx.doi.org/10.1175/JPO-D-12-057.1

Munk, W. H. and Palmen, E. (1951), Note on the Dynamics of the Antarctic Circumpolar

Current. Tellus, 3: 53–55. doi:10.1111/j.2153-3490.1951.tb00776.x

Orsi, A. H., T. Whitworth III, W. D. Nowlin Jr. (1995), Deep Sea Research Part I: Oceanographic Research Papers, 42 (5) 641-673, doi: 0967-0637(95)00021-6.

Rintoul, S. R., and S. Sokolov (2001), Baroclinic transport variability of the Antarctic Circumpolar Current south of Australia (WOCE repeat section SR3), Journal of Geophysical Research, 106(C2), 2815-2832, doi: 0148-0227/01/2000JC900107.

Roemmich, D., and J. Gilson (2009), The 2004-2008 mean and annual cycle of temperature, salinity, and steric height in the global ocean from the Argo Program, Progress in Oceanography, 82, 81-100, doi: 10.1016/j.pocean.2009.03.004.

Swart, S., Speich, S., Ansorge, I. J., Goni, G. J., Gladyshev, S., & Lutjeharms, J. R. (2008). Transport and variability of the Antarctic Circumpolar Current south of Africa. Journal of Geophysical Research: Oceans, 113(C9).

Weijer, W., S. Gille, and F. Vivier, (2009). Modal Decay in the Australia–Antarctic Basin. J. Phys. Oceanogr., 39, 2893–2909, doi: 10.1175/2009JPO4209.1.

Weijer, W. (2010), An almost-free barotropic mode in the Australian-Antarctic Basin, Geophys. Res. Lett., 37, L10602, doi:10.1029/2010GL042657.

Whitworth III, T., Nowlin Jr, W. D., & Worley, S. J. (1982). The net transport of the Antarctic circumpolar current through Drake Passage. Journal of Physical Oceanography, 12(9), 960-971.

Whitworth, T., III (1983), Monitoring the transport of the Antarctic Circumpolar Current at Drake Passage, *J. Phys. Oceanogr., 13*, 2045–2057.

Whitworth, T., III, and R. G. Peterson (1985), Volume transport of the Antarctic Circumpolar Current from bottom pressure measurements, *J. Phys. Oceanogr., 15*, 810–816.

Wunsch, C., and E. M. Gaposchkin (1980), On using satellite altimetry to determine the general circulation of the oceans with application to geoid improvement, Reviews of Geophysics and Space Physics, 18(4), 725-745.

Wunsch, C., P. Heimbach (2007), Practical global oceanic state estimation, Physica D: Nonlinear Phenomena, Volume 230, Issues 1–2Pages 197-208, ISSN 0167-2789

Appendix A

Chapter 2 - Article

AGU PUBLICATIONS

JGR

Journal of Geophysical Research: Oceans

RESEARCH ARTICLE
10.1002/2014JC009853

Southern Ocean velocity and geostrophic transport fields estimated by combining Jason altimetry and Argo data

Michael Kosempa[1] and Don P. Chambers[1]

[1]College of Marine Science, University of South Florida, St. Petersburg, Florida, USA

Key Points:
- We compute transport time series of the Southern Ocean
- Velocity fields have been validated against Argo trajectories
- Results are empirically determined

Correspondence to:
M. Kosempa,
mkosempa@mail.usf.edu

Citation:
Kosempa, M., and D. P. Chambers (2014), Southern Ocean velocity and geostrophic transport fields estimated by combining Jason altimetry and Argo data, *J. Geophys. Res. Oceans*, *119*, 4761–4776, doi:10.1002/2014JC009853.

Received 24 JAN 2014
Accepted 9 JUL 2014
Accepted article online 14 JUL 2014
Published online 5 AUG 2014

Abstract Zonal geostrophic velocity fields above 1975 dbar have been estimated for the Southern Ocean from 2004 into 2011 based on sea surface topography observed by Jason altimetry and temperature/salinity measured by Argo autonomous floats. The velocity at 1000 dbar estimated with the method has been compared to Argo drift trajectory at the same pressure level available from the Asia Pacific Data Research Center (APDRC). The inferred velocities agree with those from the Argo drift within the estimated sampling error of the latter, but have fewer gaps in space and time. The velocity has also been integrated from depth to surface to determine the mean and time-variable zonal geostrophic transport in the Southern Ocean between 29.5°S and 58.5°S, primarily in the South Atlantic and South Indian Ocean basins, due to limitations in coverage of Argo. Analysis shows errors can be reduced by >70% by averaging gridded results over wide areas. Zonal transport averaged over the entire Indian Ocean basin shows a significant correlation with the Antarctic Oscillation (AAO) at low frequencies: transport is higher than normal during a positive phase of the AAO, and lower during the negative phase.

1. Introduction

There has been considerable discussion in recent literature about the effect of climate change on winds and transport in the Southern Ocean. Large-scale climate models predict a poleward movement and strengthening of the westerly winds over the Southern Ocean in a warming world plus depletion of polar stratospheric ozone [e.g., *Fyfe and Saenko*, 2006]. Both effects have been shown to lead to increased transport and a southward shift of the Antarctic Circumpolar Current (ACC) in climate models [e.g., *Fyfe and Saenko*, 2006]. However, experiments with eddy-resolving models find increased westerlies in the Southern Ocean, leading to more energetic eddy variability with no significant trends in transport through the Drake Passage [e.g., *Hallberg and Gnanadesikan*, 2006]. Observations of ACC transport also suggest that the long-term trends in transport are much smaller than what large-scale models predict, and there is no observational evidence for a significant trend [*Gille*, 2008; *Böning et al*., 2008; *Cunningham et al*., 2003; *Rintoul and Sokolov*, 2001; *Rintoul et al*., 2002]. The lack of an apparent trend may be due to the limited number of observations, drift in the models, the current having reached the "eddy saturation limit" [*Hallberg and Gnanadesikan*, 2001], or from a compensating signal caused by freshwater and/or heat fluxes south of the ACC [e.g., *Marshall and Radko*, 2003].

Thus, there is still a significant need to understand the time-variable transport of the Southern Ocean. Although most of the transport has been shown to be geostrophic [*Whitworth and Peterson*, 1985], observations are challenging because it is not measured directly and uncertainties are often underestimated [*Cunningham et al*., 2003]. Integrating currents over the water column and along a transect allows one to compute the transport across a plane, e.g., through the Drake Passage [e.g., *Cunningham et al*., 2003], or the choke point south of Tasmania [*Rintoul and Sokolov*, 2001; *Rintoul et al*., 2002]. Other estimates are based on combinations of transects across the Southern Ocean [e.g., *Gille*, 2008; *Böning et al*., 2008], or using data collected from moorings present over a short period of time, typically no longer than a year [e.g., *Whitworth*, 1983; *Whitworth and Peterson*, 1985; *Chereskin et al*., 2009]. Velocity profiles are traditionally inferred from CTD casts, where the temperature/salinity is converted to density via an equation of state, allowing one to compute relative geostrophic currents between each cast location.

The major limitation of this method is that these velocity profiles are relative to a reference current that is often unknown. Significant error can be introduced by not knowing the reference current at any level. The

current at the deepest common level (DCL) is typically assumed to be zero, which is an invalid assumption in the ACC. The currents in the deepest layers of the ACC are not zero and are sometimes flowing in the opposite direction based on calculations from lowered acoustic Doppler current profilers (LADCPs) made along with CTD casts [*Cunningham et al*., 2003; *Renault et al*., 2011], shipboard ADCP data closer to the surface [*Donohue et al*., 2001], or with Current and Pressure Recording Inverted Echo Sounders [*Chereskin et al*., 2009]. Estimated near-bottom velocities range from 10 to 20 cm s^{-1} [*Cunningham et al*., 2003], and to as high as 60 cm s^{-1} during cyclogenesis events [*Chereskin et al*., 2009].

The sensitivity of the volume transport calculation to the reference velocity can be illustrated by a change in the current at 3000 m depth of only 1 cm s^{-1} per year across the width of the ACC ($\sim 10^{\circ}$ of latitude), which amounts to a transport trend of 30 Sv yr^{-1} (1 Sv = 10^6 m^3 s^{-1}). Ignoring the reference current by setting the value to zero limits observational accuracy of ACC transport, leading to biases of nearly 20% of a commonly accepted value of 135 Sv [e.g., *Cunningham et al*., 2003]. Thus, the current at some reference level at the time the temperature/salinity measurements are made is vital to quantifying changes in transport.

More than 30 years ago, *Wunsch and Gaposchkin* [1980] proposed a method (hereafter WG80) to resolve this problem by combining hydrographic data with satellite-obtained sea surface height (SSH) data that has been combined with a geoid. They contended that currents estimated from SSH measured by satellite altimeters relative to a geoid determined from a satellite gravity mission could serve as the reference to compute velocity profiles at depth. This choice of reference is optimal since a geoid is defined as a level of no motion in a gravitational sense. WG80 proposed that the mean and variable transports of the geostrophically balanced systems could be measured on large scales for the first time and on an ongoing basis using this reference current along with accurate temperature/salinity measurements from hydrographic sections.

When originally proposed, the uncertainties of both SSH and the geoid were too high to perform better than assuming zero current at some reference level. There were no ongoing satellite altimeter missions and no dedicated satellite gravity mission to improve the geoid. Although the accuracy of SSH improved dramatically as part of the TOPEX/Poseidon prelaunch and postlaunch activities [e.g., *Chelton et al*., 2001], the accuracy of the geoid was not sufficient to recover surface geostrophic currents with any accuracy [*Stammer and Wunsch*, 1994; *Tapley et al*., 1994; *Ganachaud et al*., 1997]. The SSH was, however, accurate enough to estimate time-variable surface geostrophic currents on both the large scale [e.g., *Fu and Chelton*, 2001] and mesoscale [*Le Traon and Morrow*, 2001], so research focused on evaluating only the variable surface currents and transports.

Geoid models have improved by an order of magnitude in the last decade with the launch of the Gravity Recovery and Climate Experiment (GRACE) in 2002 and the Gravity field and steady state Ocean Circulation Experiment (GOCE) in 2009. *Tapley et al*. [2003] used a preliminary GRACE geoid based on only 100 days of observations to recover zonal surface currents with an accuracy of better than 5 cm s^{-1} RMS over length scales longer than 500 km, compared to accuracies of order 10 cm s^{-1} RMS or larger using previous geoids. Subsequent improvements in geoids have led to even smaller uncertainties over smaller spatial scales (approaching 100 km) using preliminary releases of GRACE/GOCE combination geoids [*Bingham et al*., 2011; *Knudsen et al*., 2011] or geoids that combine GRACE with terrestrial gravity measurements [*Pavlis et al*., 2012].

The first effort to use this method was by *Cadden et al*. [2009]. Their study applied WG80 to three point locations in the equatorial Indian Ocean and compared results to absolute velocity measured by acoustic Doppler current profilers (ADCP). They combined TOPEX/Poseidon (T/P) and Jason-1 altimetry with the GGM02 geoid model based on GRACE data [*Tapley et al*., 2005]. Their use of monthly climatological profiles of T/S from the World Ocean Atlas 2005 (WOA05) [*Antonov et al*., 2006; *Locarnini et al*., 2006] introduced sampling inconsistency as the ADCP and altimetry products were averaged over 10 day periods and the T/S data at depth were based on mapped climatologies, so did not contain any interannual fluctuations, only the mean seasonal variation. *Cadden et al*. [2009] identified the leading causes of error as incompatibility of temporal and spatial resolution between the observations and computing geostrophic currents near the equator where geostrophy breaks down. Their experiment did find qualitative agreement between the calculated and measured velocities at depth despite these limitations.

More recent studies have explored the technique using subsurface density from either model state estimates or estimated from projections from surface data. *Griesel et al*. [2012] compared four mean dynamic

ocean topography products combined with a climatology and density from the Southern Ocean State Estimate (SOSE) model to investigate mean transport in the Southern Ocean. They found altimetry and geoid only versions of mean dynamic ocean topography outperformed combined "hybrid" versions of topography when compared to transport from the SOSE model. The version based on the Earth Gravitational Model 08 (EGM08) [*Pavlis et al*., 2012] performed the best. However, the transport calculated with all mean dynamic topography models tested (EGM08, CNES-CLS09, GGM02C, and MN05) still all had large mass discontinuities (i.e., substantial differences in integrated transport) between basins.

Mulet et al. [2012] created subsurface T/S data by regressing SSH and sea surface temperature anomalies against Argo T/S data to 1500 m depth and then constructed velocity fields using the WG80 method. They used the data to study variations in the Atlantic Meridional Overturning Circulation (AMOC) and validated results against Argo float displacements at 1000 m depth. They found a mean standard deviation of the differences in currents at 1000 m in the Atlantic of 5.9 cm s^{-1} for the zonal component and 5.8 cm s^{-1} for the meridional, with no significant bias.

There have been similar investigations with projections of surface altimetry anomalies onto static modes determined from historical in situ observations. The method follows the work of *Sun and Watts* [2001], who projected historical CTD data onto baroclinc stream functions to determine three-dimensional modes parameterized by pressure, geopotential height, and longitude, called Gravest Empirical Modes (GEMs). GEMs are computed as mean, time-invariant modes. *Meijers et al*. [2010] determined Gravest Empirical Modes to establish static ACC subsurface modes using WOCE and Argo data. They then projected SSH anomalies onto the static modes to determine time-variable subsurface density. They derived velocity fields using the WG80 method from the surface to 2000 dbar using mapped SSH anomalies from AVISO [*Ducet et al*., 2000] and the Rio05 mean dynamic topography map [*Rio and Hernandez*, 2004]. Their fields were compared by spatially interpolating to Argo drift velocity estimates, with favorable results. Their RMS between velocity products ranged from 4.8 to 14.8 cm s^{-1} within the subantarctic front.

While these studies have shown promise in deriving subsurface currents from a combination of surface altimetry, a geoid, and subsurface density fields, all have noted potential issues. One issue is the use of a static mode for projection. Another potential issue is the assumption the sea level variations are dominantly steric [*Meijers et al*., 2010]. Although the later assumption is generally true in the midlatitudes and tropics, there have been numerous studies showing that barotropic signals in the high latitudes (particularly the Southern Ocean) form a significant fraction of sea level variability, on time scales ranging from a few days to several years [e.g., *Vivier et al*., 2005; *Bonin and Chambers*, 2011; *Quinn and Ponte*, 2012; *Piecuch et al*., 2013]. Other noted potential issues are the difference in smoothing between the mean dynamic topography, the SSH anomalies, and subsurface density data [*Meijers et al*., 2010; *Mulet et al*., 2012; *Griesel et al*., 2012], and large excursions in the upper ocean, due primarily to projecting surface data with signals from eddies into the subsurface using static modes or regressions that do not fully capture the vertical structure of eddies [e.g., *Meijers et al*., 2010; *Mulet et al*., 2012].

To address several of these issues, we compute the velocity field using coherently mapped surface altimetry, mean dynamic topography, and Argo T/S data rather than projecting higher resolution altimetry onto static vertical modes and lower resolution mean dynamic topography. Although our mapping will not be as high a resolution as some other studies due to the limitation of Argo data, it will be more consistent, and we demonstrate it will reduce the signal of surface mesoscale eddies on subsurface velocity data and lead to lower uncertainty of velocity estimates at 1000 dbar.

We focus our initial experiments on computing the zonal geostrophic velocity field in the Southern Ocean, where velocities at depth are large. We compare the currents estimated at 1000 dbar (the parking depth of Argo floats) to estimates derived from the drift of Argo floats reported at the Asia Pacific Data Research Center (APDRC) [*Lebedev et al*., 2007]. We expand the results of *Meijers et al*. [2010] and *Griesel et al*. [2012] to compute time series of transport variability at two choke points in the Southern Ocean and across the South Indian Ocean.

Section 2 describes the method to combine SSH from altimetry, a geoid, and T/S profiles to derive currents at depth and to compute the volume transport, along with the data sets used. Section 3 describes comparisons with Argo drifts, section 4 describes evaluation of mean and time-variable transport at several locations in the Southern Ocean from the velocity fields along with an uncertainty analysis, and section 5

concludes with an assessment of the method and future work. Unless otherwise stated, when transport is referred to in this paper, zonal geostrophic transport is meant. Ekman transport, which is primarily meridional in the Southern Ocean, is not considered.

2. Methods and Data

WG80 computes subsurface geostrophic velocity by manipulating two surface velocity calculations. One surface velocity is determined from an absolute dynamic topography ($\eta_{absolute}$), from satellite altimetry sea surface height (SSH) data and a geoid (N). The other surface velocity is determined from a relative dynamic topography ($\eta_{relative}$) based on T/S data at standard pressure levels (P_1, P_2, P_3, . . ., P_n),

$$\eta_{absolute}(x,y,t) = SSH(x,y,t) - N(x,y),$$
$$\eta_{relative}(x,y,z,t) = \frac{1}{g(y)} \int_{P_z}^{P_{surface}=0} \frac{dP}{\rho(T,S,P)}, \tag{1}$$

where x is zonal position (i.e., longitude), y is the meridional position (i.e., latitude), z is depth, t is time, g is acceleration due to gravity (varying by latitude due to the oblateness of the Earth), P is pressure, T is temperature, S is salinity, and ρ is density. Note that the relative topography is dependent on the reference depth (pressure) the integration starts at. Density is computed from temperature, salinity, and pressure via the thermodynamic Equation of Seawater (*TEOS-2010*) from the Gibbs Seawater Oceanography Toolbox [*McDougall and Barker*, 2011]. N is the time-averaged geoid.

The geostrophic velocity components at the surface are then determined from the gradient of absolute topography

$$u_{surface} = -\frac{g(y)}{f}\frac{\delta\eta_{absolute}(x,y,t)}{\delta y},$$
$$v_{surface} = \frac{g(y)}{f}\frac{\delta\eta_{absolute}(x,y,t)}{\delta x}, \tag{2}$$

where f is the Coriolis parameter, u is the zonal (east-west) current, positive eastward, and v is the meridional (north-south) current, positive northward.

Alternatively, one needs to know the current at the reference level to compute the surface current from the gradient of relative topography:

$$u_{surface} = -\frac{g(y)}{f}\frac{\delta\eta_{relative}(x,y,z,t)}{\delta y} + u(z),$$
$$v_{surface} = \frac{g(y)}{f}\frac{\delta\eta_{relative}(x,y,z,t)}{\delta x} + v(z). \tag{3}$$

Substitution and rearrangement of equations (2) and (3) allows one to calculate the zonal and meridional velocity at depth corresponding to the starting depth in the integral of equation (1):

$$u(z) = -\frac{g(y)}{f}\left(\frac{\delta\eta_{absolute}(x,y,t)}{\delta y} - \frac{\delta\eta_{relative}(x,y,z,t)}{\delta y}\right),$$
$$v(z) = \frac{g(y)}{f}\left(\frac{\delta\eta_{absolute}(x,y,t)}{\delta x} - \frac{\delta\eta_{relative}(x,y,z,t)}{\delta x}\right). \tag{4}$$

Thus, utilizing equation (4) and a combination of Argo-inferred relative velocity fields and Jason-observed absolute velocity, one can compute the geostrophic zonal velocity field as a function of depth, using an integral (equation (1)) over variable depths. In this study, these velocities will be denoted $u_{\text{jason-argo}}(z)$. One can also assume the velocity at depth is zero, then solve for the surface current from equation (3). This is denoted $u_{\text{argo}}(0)$. Finally, if any independent measure of the current at z is known ($u_{\text{trajectory}}(z)$), this can be used as a reference velocity in equation (3) to obtain a surface current, $u_{\text{argo}+\text{trajectory}}(0)$.

Gradients in equations (2) and (3) are computed using a center difference. Integrating velocity profiles meridionally (y_{south} to y_{north}) and vertically (z) determines the zonal volume transport (T) above the deepest measured level at a particular transect at any time by

$$T(x,t) = \int_{y_{south}}^{y_{north}} \int_{z_{reference}}^{z_{surface}=0} u(x,y,z,t)\ dz\ dy. \tag{5}$$

In practice, $\eta_{absolute}$ is computed in terms of a time-variable topography ($\Delta\eta_{absolute}$) relative to a static mean sea surface (*MSS*) and a time-mean dynamic topography ($\bar{\eta}_{absolute}$) so that

$$\begin{aligned} \Delta\eta_{absolute}(x,y,t) &= SSH(x,y,t) - MSS(x,y), \\ \bar{\eta}_{absolute}(x,y) &= MSS(x,y) - N(x,y), \\ \eta_{absolute}(x,y,t) &= \bar{\eta}_{absolute}(x,y) + \Delta\eta_{absolute}(x,y,t). \end{aligned} \tag{6}$$

The 1 Hz along-track sea surface height data from Jason-1 and Jason-2 geophysical data records (GDR), Version C [*Picot et al.*, 2012] are used to compute sea level anomalies (SLAs); the SSH data are corrected for all recommended geophysical and atmospheric corrections. A high-resolution MSS computed by the Danish National Space Center [*Andersen and Knudsen*, 2009] has been utilized instead of the model on the GDR to compute SLAs and the mean dynamic topography; the GDR MSS was last updated in 2001. The geoid used is constructed from the Earth Gravity Model 2008 (EGM08) [*Pavlis et al.*, 2012], which optimally combines long-wavelength gravity information from GRACE with high-resolution surface gravity data from altimetry, as well as airborne and in situ gravimeters. A mean absolute topography is constructed by differencing the geoid from the MSS (equation (6)), which has a resolution of less than 5 km at the equator. By using the same MSS to compute SLAs and the mean dynamic topography, no residual biases from different time-averaging periods of MSS models will be present.

We utilize temperature and salinity products based on Argo T/S observations that were optimally interpolated to 1° grids [*Roemmich and Gilson*, 2009]. These products are readily available at monthly intervals from 2004. The gridded Argo data are restricted to north of 60°S, so the present products preclude study of important areas such as the Drake Passage and the southern extent of the ACC in the Pacific Ocean, where strong fronts exist poleward of 60°S. All grids presented herein are shown for the zonal band between 29.5°S and 58.5°S, unless otherwise noted. The Argo data are provided with 58 pressure levels, spanning 2.5–1975 dbar. We utilize maps from January 2004 through June 2011 (90 months).

To best match the Argo gridded data, the SLAs and high-resolution mean absolute topography are mapped using the same optimal interpolation method and covariance function ($C(dist)$) as *Roemmich and Gilson* [2009]:

$$C(dist) = 0.77 * \exp\left(-(\mathrm{dist}/140.0)^2\right) + 0.23 * \exp(-\mathrm{dist}/1111.0), \tag{7}$$

where $dist = \mathrm{sqrt}(dx^2 + dy^2)$, dx is the zonal distance in km between the grid center and observation, and dy is the meridional distance. A noise-to-signal variance ratio of 0.15 was used on the diagonal to account for random noise. After mapping the monthly SLAs and mean topography separately, results are then combined as described in equation (6).

Figure 1 shows representative (July 2010) relative and absolute dynamic ocean topography (DOT). The two images have different coverage in various regions. The Argo maps do not cover marginal seas or close to coastlines. The important chokepoint of the Indonesian Throughflow, for example, is absent, and half the Drake Passage has no interpolated values. The Jason products, alternatively, have missing areas in the south that have been flagged for various quality control reasons (e.g., ice cover). Both products are missing large areas of the Southern Ocean near the Antarctic continent, although the altimeter products are interpolated to 65°S. One cannot compute integrated transport from the Antarctic continent with this product, only between latitude bands equatorward of 59°S.

The problem with ignoring currents at depth in the relative topography calculation appears in Figure 1. The gradient of the absolute topography in the Southern Ocean is much steeper than that determined from the relative topography, differing by roughly 0.5 m between 60°S and 30°S. From equation (4), one concludes a significant current exists at the reference depth to resolve this disparity. Similarly, more subtle differences can be observed in the Gulf Stream and Kuroshio regions, suggesting currents at depth in those regions, as well.

Validating the calculation requires an independent measurement of the velocity at depth. We utilize velocity products derived from drifter trajectory at Argo's parking depth [*Lebedev et al.*, 2007]. Estimated

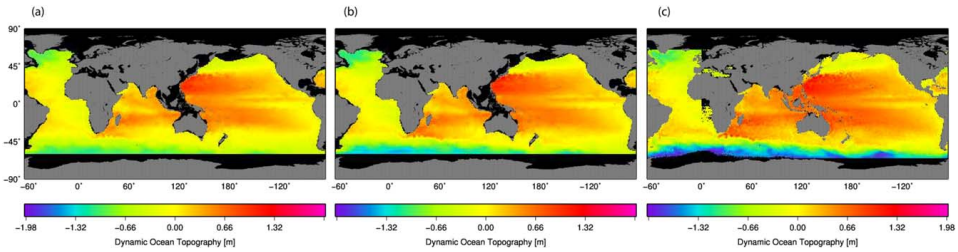

Figure 1. Dynamic ocean topography for July 2010 inferred from (a) Argo hydrographic data with a zero reference velocity at 1000 dbar, (b) with a zero velocity at 1975 dbar, and (c) from SSH relative to EGM08. Anomaly determined relative to 60 month mean between 2006 and 2011.

sampling error (one standard deviation) for this data is between 3 and 4 cm s^{-1} in most parts of Southern Ocean, although it can be as large as 8 cm s^{-1} in regions of high mesoscale variability [*Katsumata and Yoshinari*, 2010]. The highest uncertainty is in the South Pacific between 180°E and 270°E, with estimates of more than 8 cm s^{-1} [*Katsumata and Yoshinari*, 2010, Figure 13]. As the authors state, this is likely due to a combination of sparse coverage of Argo floats in this region and energetic eddy variability. Trajectory estimates are available at annual and 3 month seasonal binned averages from 2004 onward. The Argo drift products have not been interpolated for this analysis, merely binned into the same 1° grids used for the altimetry and Argo optimally interpolated data. This velocity product is only used here at the 1000 dbar level and is denoted $u_{\text{trajectory}}(1000)$.

Figure 2 shows the sampling events of $u_{\text{trajectory}}(1000)$ over 5 years, indicating limited coverage in many regions. Drift estimates are more numerous in areas of low velocity at depth and low mesoscale eddy activity; this emphasizes the difficulty in reconstructing a velocity based solely on position differences in a dynamic current field. The majority of drift estimates are located north of the ACC where deep currents are significantly slower than along the fronts of the ACC. There are typically fewer than 12 observations south of 45°S during the 5 year period. Many areas have as few as 6–8, while most of the area poleward of 58°S has less than four total trajectory fixes per 1° bin over the time period.

Figure 2 shows observations are available south of 60°S, implying the potential to remap Argo temperature and salinity data for further Southern Ocean studies in the future. Note that many more Argo T/S profiles are available over this time for mapping than are used in the drift trajectory, due to editing and the requirement to have two profiles within a certain time to establish a velocity.

Output from the Southern Ocean State Estimation (SOSE) [*Mazloff et al.*, 2010] is also used to quantify the uncertainty associated with mapping data, which will smooth currents along fronts over a larger area. SOSE produces zonal velocity products at 1/6° spatial resolution at 5 day time steps. Six months of SOSE data, spanning the first half of 2008, were utilized by integrating zonal velocity to produce transport fields at 5 day resolution. The SOSE output was also mapped to 1° grids using a Gaussian weighted average with a 150 km roll-off (see section 4.2).

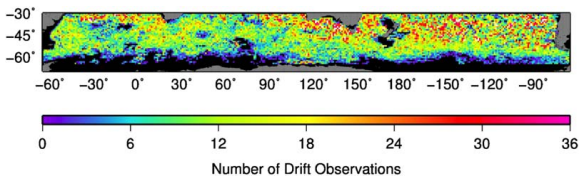

Figure 2. Number of velocity observations in each 1° × 1° bin determined from Argo float trajectories used to generate $u_{\text{trajectory}}(1000)$ between 2006 and 2011.

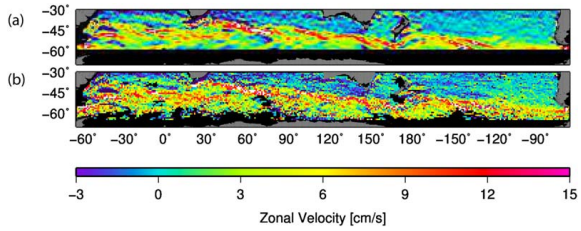

Figure 3. (a) $u_{\text{jason-argo}}$ and (b) $u_{\text{trajectory}}$ (2006–2011) average zonal currents at 1000 dbar. Velocity is positive in the eastern direction.

3. Comparison of Currents at 1000 dbar

Five year means (2006–2010) of $u_{\text{jason-argo}}(1000)$ compared to $u_{\text{trajectory}}(1000)$ show comparable currents at similar locations, indicating qualitative agreement (Figure 3). As examples, the Brazil-Malvinas Confluence region and frontal positions in the southeastern Atlantic basin are apparent in both $u_{\text{jason-argo}}(1000)$ and $u_{\text{trajectory}}(1000)$. The magnitudes are consistent with previous studies that have found strong mean currents of order 10–20 cm s^{-1} at 1000 dbar in the Drake Passage along the major fronts, based on shipboard ADCPs [*Firing et al*., 2011].

The mean of common points between products is 1.9 cm s^{-1} for $u_{\text{jason-argo}}(1000)$ and 2.3 cm s^{-1} for $u_{\text{trajectory}}(1000)$, suggesting a bias of -0.4 cm s^{-1}, with $u_{\text{jason-argo}}(1000)$ being lower than $u_{\text{trajectory}}(1000)$. The standard error of the mean is 0.04 cm s^{-1} for $u_{\text{jason-argo}}(1000)$ and 0.06 cm s^{-1} for $u_{\text{trajectory}}(1000)$, signifying this is a significant bias (uncertainty ± 0.07 cm s^{-1} based on RSS of standard errors). The standard deviation of the difference is 3.9 cm s^{-1}. This value of 3.9 cm s^{-1} is an upper bound for the error in the mean currents obtained by the WG80 method over the region. If one uses an average sampling error for $u_{\text{trajectory}}(1000)$ of 3.0 cm s^{-1} [*Katsumata and Yoshinari*, 2010], this suggests the error in our mean currents estimated by the WG80 method over the region is likely 2.5 cm s^{-1}.

For a different comparison, two coordinates with high temporal coverage by $u_{\text{trajectory}}(1000)$ are compared (Figure 4). There are 17 $u_{\text{trajectory}}(1000)$ values over 20 seasons at both coordinates. "Coordinate 1" (138°E, 40°S) is south of Australia, north of the ACC. "Coordinate 2" (148°E, 51°S) is closer to the ACC, located south of Tasmania. Note that these two points represent locations of very different mean currents. "Point 1" is north of the subtropical front, where currents are low, whereas "Point 2" is closer to the polar front, where mean currents are high.

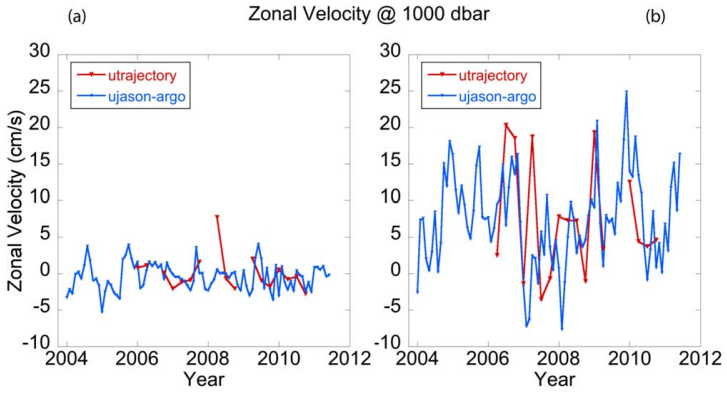

Figure 4. Velocity time series from (a) $u_{\text{jason-argo}}(1000)$ and (b) $u_{\text{trajectory}}(1000)$ at two coordinates. (left) 138°E, 40°S. (right) 148°E, 51°S.

Table 1. Velocity (cm s^{-1}) Time Series Statistics From Coordinates 1 (138°E, 40°S) and 2 (148°E, 51°S) $u_{jason\text{-}argo}$ and $u_{trajectory}$

	$u_{jason\text{-}argo}$ Coordinate 1	$u_{trajectory}$ Coordinate 1	$u_{jason\text{-}argo}$ Coordinate 2	$u_{trajectory}$ Coordinate 2
Mean velocity	−0.48	0.00	7.41	7.87
Standard deviation	1.83	2.40	6.25	7.79
Standard deviation difference	2.11		7.51	
Standard error of mean	0.19	0.58	0.66	1.91

Both time series display an extreme velocity in $u_{trajectory}(1000)$ relative to $u_{jason\text{-}argo}(1000)$, using a criteria of a difference larger than 10 cm s^{-1}. Sampling deficiencies of $u_{trajectory}(1000)$ are also apparent; several periods have no drift estimates, unlike $u_{jason\text{-}argo}(1000)$, which has monthly data availability. The mean velocities in both regions agree to within 0.5 cm s^{-1}, although the standard error for the time series using altimetry and Argo T/S profiles is lower due to having more observations (Table 1). These results are in close agreement with the grid-level validation. The mean and standard deviations are higher for both $u_{jason\text{-}argo}(1000)$ and $u_{trajectory}(1000)$ for the grid located in the ACC, as one would expect.

Figures 5 and 6 show the standard deviation of the differences and correlation coefficient, respectively, between $u_{jason\text{-}argo}(1000)$ and $u_{trajectory}(1000)$ for 5° grids using the 5 years of trajectory data. The standard deviation is up to 6 cm s^{-1} in some regions of the ACC, but these are isolated to a few grids; in general, the standard deviation is between 2 and 4 cm s^{-1}. The products ($u_{jason\text{-}argo}(1000)$ and $u_{trajectory}(1000)$) are significantly correlated over much of the basin, with values as high as 0.7–0.8. Correlations between products remain significant even in areas of high variability such as the Agulhas region. This is a similar result to that of *Meijers et al.* [2010], who used drifts at multiple depth levels. An area of significant difference is west of the Prime Meridian, where the present study has found significant correlation between $u_{jason\text{-}argo}(1000)$ and $u_{trajectory}(1000)$, whereas *Meijers et al.* [2010, Figure 16] do not.

These analyses indicate that subsurface currents computed from a combination of altimetry and Argo T/S profiles are at least as accurate as those computed from Argo drift trajectories. Moreover, the method can be used to better estimate velocity profiles at monthly intervals from the surface to 1975 dbar and the estimated uncertainty is slightly lower than that based on the trajectory method.

4. Estimates of Transport

The following sections will describe estimates of the mean and time-variable transport computed from the velocity data discussed in section 3. Section 4.1 will describe the method used to define boundaries for integration, section 4.2 will estimate error bars based on uncertainty in the reference velocity, mapping error, and uncertainty in currents at each level, and section 4.3 will discuss estimates of mean transport. Finally, section 4.4 will examine time-variable transport in the Indian Ocean sector of the ACC, in particular, the relationship to variability of the Southern Annual Mode (SAM), or the Antarctic Oscillation (AAO).

4.1. Defining Boundaries of Integration

Before integrating to obtain transport, it is useful to consider the boundaries that define the persistent eastward flow. Persistence is a natural defining characteristic of the northern and southern boundaries of the

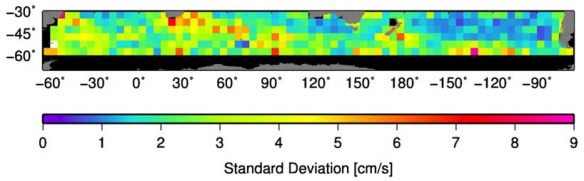

Figure 5. Standard deviation of seasonal (3 month averages) $u_{jason\text{-}argo}(1000)$ minus $u_{trajectory}(1000)$ over 5 year period (20 seasons) based on data in 5° grids.

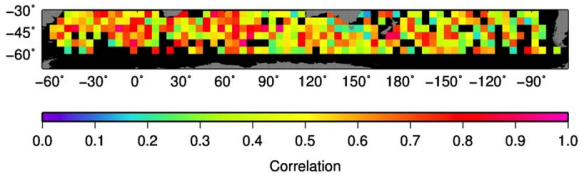

Figure 6. Correlation between seasonally averaged $u_{\text{jason-argo}}(1000)$ and $u_{\text{trajectory}}(1000)$ over 5 year period (20 seasons) in 5° grids. Squares below 95% confidence have been masked.

ACC, much like using gradients of dynamic topography or density from hydrographic data [e.g., *Orsi et al.*, 1995].

Persistence can be easily computed by summing the grid cells computed in section 3 that have eastward flow at each longitude, latitude, depth, and time, and then dividing by the total available. This has been done with the $u_{\text{jason-argo}}(z)$ data to create a histogram to identify regions of persistent eastward flow above 1975 dbar (Figure 7).

There are alternating bands of high and low persistence north of the ACC (Figure 7), such as those between Australia and New Zealand or in the South Pacific. These features are consistent with what have been referred to as zonal jets [*Galperin et al.*, 2004] in the circulation that have been observed in other in situ and satellite data [e.g., *Maximenko et al.*, 2009], but are much weaker in persistence than the stronger ACC circulation.

Because the subtropical front is more variable both in time and location [*Graham et al.*, 2012] and has lower persistence than the fronts to the south, an algorithm was developed to identify the location of persistent transport defining the ACC south of the subtropical front based on the persistence over 90 months (Figure 7). The algorithm allows one to systematically isolate the plateaus of persistence, i.e., the transition from low persistence to high persistence consistent with the eastward zonal geostrophic currents at all depths of the ACC. The algorithm defines the ACC as contiguous latitudes at or above 60% persistence and requiring at least one of these latitudes to be at least 94.5%. The minimum value of 94.5% was required (instead of 95%) to include all meridians. The 60% was chosen somewhat arbitrarily, but is necessary to identify the transition. Tightening the definition to minimum value of 70% versus 60% will not make a noticeable change to the spatial identification.

4.2. Transport Uncertainty

High-resolution model output from SOSE (section 2) has been used to investigate the effect of smoothing in the mapping of altimetry and T/S fields on the integrated volume transport. This was done to better understand the impact of moving from mesoscale processes to the large-scale background flow under investigation.

A Gaussian smoother with a 150 km roll-off was used to remap the output of the SOSE model to a 1° grid because the optimal interpolation (OI) is computationally slow with large amounts of data. This Gaussian smoother best matches the OI, based on an analysis of the residuals over a small region south of Africa where eddy kinetic energy is the highest. Residuals of the original data relative to the mapped data tended

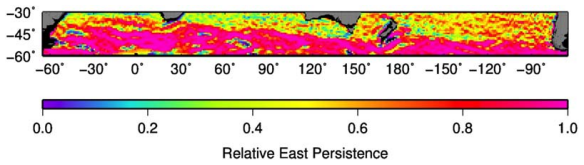

Figure 7. Persistence of eastward current determined from $u_{\text{jason-argo}}(z)$ using 58 depth levels and 90 months.

Table 2. Bias, Standard Deviation (σ), and Correlation (ρ) Between Gaussian-Smoothed and Original SOSE Cumulative Transport, for Three Regions of Differing Eddy Kinetic Energy and With Three Zonal Averaging Areas

	1°			11°			21°		
Zonal Averaging Region	Bias (Sv)	σ (Sv)	ρ	Bias (Sv)	σ (Sv)	ρ	Bias (Sv)	σ (Sv)	ρ
Low EKE (345°E)	−3.4	3.6	0.97	−1.2	1.4	0.99	−0.7	1.2	0.99
Med EKE (149°E)	22.4	5.0	0.95	1.2	1.5	0.99	−2.0	1.2	0.99
High EKE (21°E)	−3.3	8.4	0.76	−4.6	2.8	0.97	−1.1	1.9	0.98

to be mostly random with the smallest spatial lag-1 autocorrelation at 150 km roll-off, which is close to the mesoscale portion of the covariance function used in the OI (equation (7)).

The transport was integrated over the full-depth water column and across the ACC defined using the algorithm described in section 4.1. This integration produced time series of both the raw SOSE grids and the 1° mapped grids. The cumulative transports at three locations were compared. The locations were selected based on the level of eddy kinetic energy (EKE) derived from mapped altimetry [e.g., *Ducet et al*., 2000]. These were at the African chokepoint (21°E) for high EKE, 345°E for low EKE, and 149°E for moderate EKE. Statistics were computed using differing levels of averaging over longitude widths centered at these meridians, ranging from no averaging to 21° in longitude (Table 2).

The Gaussian smoothed transport is biased differently at each region, with values as high as 22 Sv in the region deemed moderate EKE (Table 2). Along a single 1° transect the standard deviations of the residuals range from 3.6 to 8.4 Sv, with the smallest residuals occurring where EKE is low, and the largest where EKE is high (Table 2). With averaging over longitude bands, however, the mapping error is reduced, approximately by 1/sqrt(n), where n is the number of 1° transects averaged, which indicates more or less random errors from one transect to the next. After averaging over 21° of longitude, biases are of the order of 2 Sv and standard deviations range from 1.2 to 1.9 Sv (Table 2). Although high EKE regions still have slightly higher mapping errors, they are not substantially higher. The high correlations suggest that the mapped transport can reproduce the time-variable integrated transport reasonably well. The standard deviations provide representative error estimates attributed to mapping of ∼5 Sv for a calculation along a 1° meridian, 1.5 Sv when averaged over 11° of longitude, and 1.2 Sv when averaged 21°, using the medium EKE values, which is consistent with the level of EKE in the Indian Ocean where future time-variable transport calculations are conducted (section 4.4).

There are two other sources of uncertainty that must be considered. The first is larger and arises from the uncertainty in the reference velocity multiplied by the full depth to 1975 dbar. Using uncertainties of 2.5 and 3.0 cm s^{-1} in the reference velocities (section 3) of $u_{jason\text{-}argo}(1000)$ and $u_{\text{trajectory}}(1000)$ yields error estimates of 30.1 and 36.1 Sv, respectively, across a 30° latitude width, or 17.4 and 20.8 Sv for 10°, the average width of the ACC. This assumes no correlation of errors from one grid cell to the next, and is the uncertainty for a single 1° transect.

The second source of error is from the geostrophic shear at each level. Since the reference velocity $u_{jason\text{-}argo}(1000)$ has an estimated uncertainty of 2.5 cm s^{-1} and includes the errors in both the shear computed from altimetry and the density from Argo, we use this as the estimate of uncertainty for each level. Assuming no correlated errors between depths, the uncertainty attributed to velocity shear uncertainty is 5.0 Sv for integrated transport over 30° of latitude, or 2.9 Sv for 10° of latitude. Thus, the uncertainty in the measurement of the reference velocity dominates both the mapping error and uncertainty in currents at each level. Assuming the uncertainties in velocity shear, mapping, and reference current are uncorrelated, the uncertainty for transport integrated over 30° of latitude is 30.8 Sv for transport calculated relative to $u_{jason\text{-}argo}(1000)$ and 36.7 Sv for $u_{\text{trajectory}}(1000)$ for a single 1° transect.

Reducing the north-south extent of the integration reduces the absolute uncertainty for that segment. The full ACC is observable south of Africa, and has a lateral extent of approximately 13°. The ACC south of Tasmania is not fully observable with the current products, limiting the lateral extent to just under 8°. The uncertainties across the reduced spans are again dominated by the uncertainty in the reference velocity, and are 21.9 Sv for the section of the ACC south of Africa and 15.5 Sv for the section south of Tasmania, including the uncertainty in mapping and geostrophic shear.

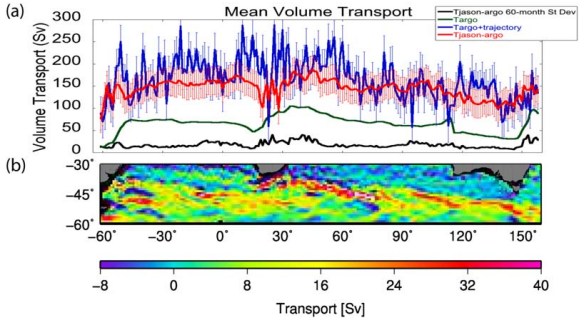

Figure 8. (a) Mean $T_{\text{jason-argo}}$, $T_{\text{argo+trajectory}}$, and T_{argo} across each longitude integrated from 1975 dbar to the surface and between 30°S and 59°S. All are total transport above 1975 dbar, using different reference currents at 1000 dbar. Error bars include uncertainty in reference velocity, geostrophic shear at each level, and mapping error as described in section 4.2. Standard deviation of $T_{\text{jason-argo}}$ also shown. (b) $T_{\text{jason-argo}}$ 60 month mean of volume transport from a depth of 1975 dbar to the surface for each 1° cell.

When transports are spatially averaged across longitudes, we assume the uncertainty is reduced by a factor of 1/sqrt(n), where n is the number of meridians averaged. This is consistent with the mapping error results (Table 2).

4.3. Mean Transport

Three different velocity fields have been produced based on a different reference velocity; zero (i.e., assuming a zero reference current at 1000 dbar), $u_{\text{jason-argo}}(1000)$, and $u_{\text{argo+trajectory}}(1000)$. The distinct fields are integrated from 1975 dbar to the surface for each month and at each coordinate to compute zonal transport for each 1° cell according to equation (5). The transport from integrating $u_{\text{argo}}(z)$ (assuming a zero reference current at 1000 dbar) is denoted T_{argo}, likewise $T_{\text{jason-argo}}$ assumes the $u_{jason\text{-}argo}(1000)$ values estimated in this study as a reference, while and $T_{\text{argo+trajectory}}$ uses the value of $u_{trajectory}(1000)$ as a reference. The vertically integrated transport for each coordinate was also integrated from 60°S to 30°S to compute the total geostrophic transport across each longitude between those latitudes (Figure 8).

There are several important differences between T_{argo}, $T_{\text{jason-argo}}$, and $T_{\text{argo+trajectory}}$. The need for a reference velocity is evident in the fact that T_{argo} is of order 50–100 Sv smaller than $T_{\text{jason-argo}}$ or $T_{\text{argo+trajectory}}$. The systematically larger transports of $T_{\text{argo+trajectory}}$, however, reflect the bias in the reference current at 1000 dbar previously noted: $u_{\text{trajectory}}(1000)$ is 0.4 ± 0.07 cm s^{-1} higher than $u_{\text{jason-argo}}(1000)$ (section 3). Converted into transport across 30° of latitude and 2000 m of depth, this is equivalent to nearly 34 Sv. Considering that the commonly accepted value for mean transport across the full-depth chokepoint south of Tasmania is 147 ± 10 Sv [*Rintoul and Sokolov*, 2001], $T_{\text{argo+trajectory}}$ appears to be biased too high, with a mean value of 165 Sv for only the upper 1975 dbar. This further suggests that $u_{trajectory}(1000)$ is biased high.

The total geostrophic transports above 1975 dbar vary substantially by longitude, more so for $T_{\text{argo+trajectory}}$ than for $T_{\text{jason-argo}}$. The difference over larger sections (e.g., the decreasing values from ~30°E to 150°E) is due mainly to including areas of westward transport north of the subtropical front and also missing areas where there is eastward transport at the southern boundary that cannot be observed due to the limitation of the Argo data. The large differences between neighboring longitudes in $T_{\text{argo+trajectory}}$, however, is caused by the large variation in the reference velocity from $u_{trajectory}(1000)$. Near 1°E both $T_{\text{argo+trajectory}}$ and $T_{\text{jason-argo}}$ have a similar transport near 150 Sv. A few degrees to the east, however, $T_{\text{argo+trajectory}}$ leaps to over 200 Sv, while $T_{\text{argo+trajectory}}$ remains stable. $T_{\text{jason-argo}}$ and $T_{\text{argo+trajectory}}$ differ by up to 100 Sv west of the tip of Africa, where the Argo drift velocity has little continuity across longitude bands. These discontinuities result from the tendency of the drift velocities to be more biased by energetic local transports associated with eddies due to the low number of observations [*Katsumata and Yoshinari*, 2010]. One should note that the meridian-to-meridian changes in mean transport from $T_{\text{argo+trajectory}}$ exceed the one standard error estimate in numerous places, whereas the differences in $T_{\text{jason-argo}}$ across the basins are all within the estimated standard error. There are also several places where the differences between $T_{\text{argo+trajectory}}$ and

$T_{\text{jason-argo}}$ differ by more than the expected error (Figure 8). Some of the differences across longitudes are undoubtedly from the nonuniform biases introduced by mapping (section 4.2).

4.4. Time-Variable Transport

As demonstrated in the section 4.2, while attenuation and smoothing of higher-resolution transport along fronts of the ACC from mapping causes biases in the calculation of total transport, variations of integrated transport can still be calculated accurately, especially when averaged over longitude (Table 2).

The persistence and volume transport for the chokepoints south of Africa (21°E meridian) and Tasmania (148°E meridian) are shown as examples of the time-variable transport that can be constructed from the $u_{\text{jason-argo}}(z)$ velocity fields along a single transect (Figure 9). The persistence of each transect shows agreement in structure between chokepoints, with eastward flow occupying a narrower band and shifted south at the Tasmanian transect relative to the African transect. The location of the subtropical, subantarctic, and polar fronts [*Orsi et al*., 1995] are indicated along the top. Note that the location of the subtropical front defined by *Orsi et al*. [1995] is substantially south of the front location defined by eastward velocity persistence south of Africa, but at the Tasmanian transect they are roughly consistent. This likely is due to the problems of defining a front south of Africa due to large variability (Figure 9).

The time series of transport for the full transect is shown along with that of the ACC alone (Figure 9). The isolation of the ACC has a dramatic impact on the African time series and a somewhat muted impact on the Tasmanian time series. Principally, the area south of Africa has major mesoscale eddy activity, caused by the interaction of the strong westward Agulhas flow and the eastward flow of the ACC fronts. This is evidenced by the highly variable transport that can be isolated based on the persistence measure.

However, when the transport anomalies are compared (Figure 10), there is no significant correlation between time series of transport anomalies south of Tasmania and Africa; all values are under 0.18 (which is not significant at $p < 0.1$), even when data are averaged over 21° of longitude. Thus, the results are unphysical as they imply a lack of mass continuity in the Indian Basin, although differences are within the expected uncertainty. This suggests that even with 21° of zonal averaging, the uncertainty in the calculation is too high to study transport variability accurately. However, part of the problem may also be due to the time-invariant boundaries used in the analysis; northward or southward migration of the frontal boundaries from the mean over time could reduce correlation. The region south of Africa will likely have a more variable northern boundary as evidenced by the difference in our estimate and that of *Orsi et al*. [1995] (Figure 9).

Further averaging to obtain the mean zonal transport variability in the ACC across the Indian Ocean may be more accurate. For a 128° average (21°E–148°E), the uncertainty should drop to 2 Sv assuming random error from one transect to another. To test whether the variations in the transport anomalies averaged over the South Indian Ocean are realistic, we compare to the Antarctic Oscillation (AAO) Index [*Mo*, 2000], which is also known as the Southern Annual Mode [*Thompson and Wallace*, 2000; *Marshall*, 2003]. The AAO reflects low-frequency variations in the mean zonal winds over the Southern Ocean, and transport through the Drake Passage is significantly correlated with it [*Meredith et al*., 2004; *Bergmann and Dobslaw*, 2012].

The AAO index is constructed by projecting the daily 700 mb height anomalies poleward of 20°S from the NCEP reanalysis model onto the leading Empirical Orthogonal Function, after removing seasonal variations [*Mo*, 2000]. There is a small and significant seasonal variation in the transport variability, but it is estimated and removed using a harmonic analysis before comparing to the AAO index (Figure 11). Although the correlation between the estimated nonseasonal transport is low at 0.29, this is significant with $p < 0.01$. However, much of the differences are associated with the high-frequency variability. When a 6 month low-pass filter is applied to both time series (Figure 11), the correlation increases to 0.51 ($p < 0.05$, accounting for the reduction in the degrees of freedom from filtering). The transport is higher than normal in 2006, 2008, and 2010, consistent with positive phases of the AAO index, and lower than normal in 2007 and 2009, consistent with the negative phase of the AAO. There is poorer agreement before 2006, possibly due the smaller number of Argo floats in the Southern Ocean before this period.

It should be noted that none of the transport time series calculated over smaller averaging areas (Figure 10) are significantly correlated with the AAO, which again suggests more spatial averaging is necessary to extract meaningful low-frequency transport variability estimates.

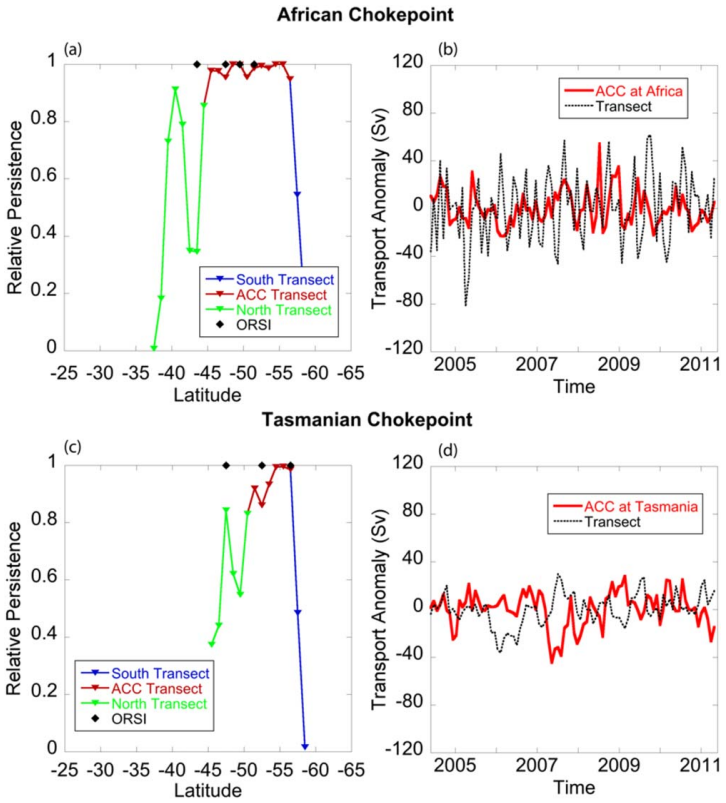

Figure 9. (left) Eastward persistence and (right) 90 month time series of zonal volume transport anomaly across the (top) African (21°E) and (bottom) Tasmanian (148°E) chokepoints. Subtropical, subantarctic, and polar (left to right) frontsfrom *Orsi et al.* [1995] are indicated along the top of persistent figures as black diamonds.

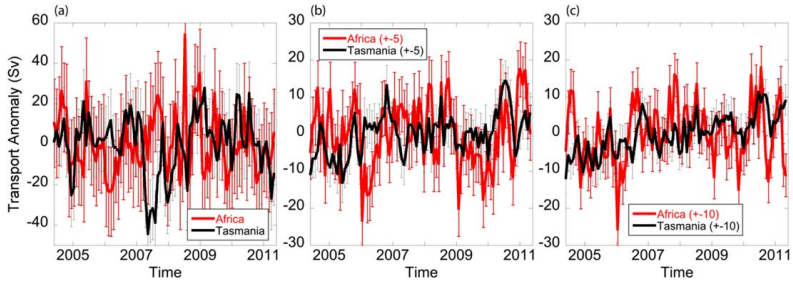

Figure 10. ACC transport anomaly time series for (a) a single 1° meridian, (b) the average of 11 meridians (±5°), and (c) the mean of 21 meridians (±10°). Error bars include uncertainty in reference velocity, geostrophic shear at each level, and mapping error as described in section 4.2, and have been reduced by 1/sqrt(*n*) to account for averaging, where *n* is the number of transects averaged.

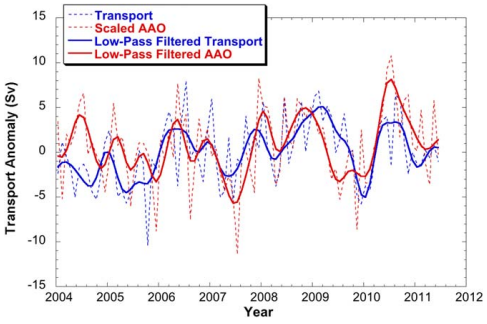

Figure 11. ACC transport anomaly time series averaged over the Indian Ocean (21°E–148°E) (blue) and the AAO index (red). The normalized AAO index (http://www.cpc.ncep.noaa.gov/products/precip/CWlink/daily_ao_index/aao/aao.shtml) has been scaled to match the variance of the transport time series. Dashed lines are monthly averages. Solid lines are after applying a 6 month low-pass filter based on a Gaussian weighted average.

5. Discussion and Future Work

Zonal geostrophic velocity fields above 1975 dbar were calculated for the Southern Ocean from 2004 into 2011 using the 30 year old method proposed by *Wunsch and Gaposchkin* [1980]. Although other studies have performed similar calculations based on either subsurface T/S from a state estimate or climatology [*Cadden et al*., 2009; *Griesel et al*., 2012] or from projections of surface data onto fixed empirical modes or regressions with historical data [*Meijers et al*., 2010; *Mulet et al*., 2012], this study uses coincident mapped T/S profiles from Argo in the calculation. Two potential issues with the *Griesel et al*. [2012] analysis are their use of truncated spherical harmonics for their geoid and smoothed dynamic topography models that were inconsistent with their higher-resolution density field, and the time periods of the mean dynamic topography were substantially different than those for the density measurements at depth. We have used similar mapping functions for all data sets to reduce problems with different resolutions, especially in the reference mean dynamic topography, and have also used the highest-resolution geoid in our processing, unlike other studies [*Cadden et al*., 2009; *Griesel et al*., 2012; *Meijers et al*., 2010].

Velocity grids from combining satellite altimetry, a geoid, and T/S profiles from the Argo program compare favorably to estimated currents at 1000 dbar based on Argo float trajectories. The standard deviation between 5 year mean velocities at 1000 dbar from our estimate and those from Argo trajectories was 3.9 cm s^{-1}, which is only slightly larger than the sampling error estimated for the drift calculation. This suggests a standard error of approximately 2.5 cm s^{-1} on our subsurface velocity estimates. Similar results were found by grouping data into 5° grids. One significant issue with using the Argo trajectories to compute reference velocities is missing data in space and time; this is minimized by combining surface currents from altimetry and gridded T/S products from Argo.

The mean transport computed from a combination of altimetry and Argo T/S data shows better mass conservation between longitudes than using Argo drift, although as *Griesel et al*. [2012] have pointed out, the conservation of mass is still poor and unrealistic. The mean transports from a combination of altimetry and Argo T/S between Africa and Tasmania data are also closer to accepted values of ACC baroclinic transport above the deepest common level of ~147 Sv [*Rintoul and Sokolov*, 2001], which suggests the Argo drifts are biased. However, although the mean transport fields are qualitatively good, they are likely biased from region to region due to the mapping required by up to 20 Sv. This can be expected to be largest in regions of high meridional property gradients and eddy kinetic energy.

The method presented here has been shown to be unable to reproduce the mean or variable transport across a single transect with any accuracy (Table 2 and Figure 10). Analysis shows the error can be reduced by >70% by averaging the gridded results over a wider zonal area, thereby increasing the confidence in both mean and time-variable transport. When averaged over 21° of longitude, there are still significant differences between the transport variations at the African and Tasmanian chokepoints, implying a failure to conserve mass. This may be attributed to inadequate isolation of the ACC using the persistence measure, incomplete data coverage on the southern side of the Tasmanian transects, contribution of signal from the subtropical front to the north, failure to consider the meridional transport component (i.e., not all the transport is zonal), or failure to cover the full chokepoint width. However, transport averaged over the entire

Indian basin (21°E–148°E) is significantly correlated with the Antarctic Oscillation at low frequencies, consistent with previous observations at the Drake Passage. This suggests that by averaging over an entire basin, one can compute realistic time-variable zonal transport with this method.

Quantifying the full uncertainty of the method will require better understanding the error introduced by sampling of eddies by the altimeters and by Argo. To do this, one can use a high-resolution model such as SOSE and sample data to altimeter and Argo float positions, then map and compare to the original model. Full understanding of uncertainties and biases is required for the continuation of the transport time series to include other hydrographic observations back to 1992, the start of altimetry records. Combining hydrographic profiles that predate Argo with the 20 year altimetry record is a key element for observing lower frequency transport in the Southern Ocean.

There are several ways to potentially improve this technique. Argo data have been mapped with a global covariance function that also includes longer-scale correlations from the tropics. Future work using this technique for the Southern Ocean should use a covariance function computed only over the region to be mapped. The covariance function should be computed for different levels, as the upper ocean temperature and salinity likely have different decorrelation scales than those for the deeper ocean. This should improve the interpolation technique to better reflect the unique covariance structure of the ACC. Remapping T/S data from Argo will also allow getting closer to the maximum latitude of Jason-1 and Jason-2 altimetry (66°) to cover the Drake Passage. Finally, using the velocity at 1000 dbar inferred from the combination of altimetry and gridded Argo T/S data may be useful in improving the estimated trajectories, both in checking for outliers and as a first guess in a mapping procedure. Future work will address all of these issues.

Acknowledgments

This research was carried out under grant NNX13AG98G from the NASA Ocean Surface Topography Science Team. The Argo data were collected and made freely available by the International Argo Program and the national programs that contribute to it. The Argo program is part of the Global Ocean Observing System. Jason-1 and Jason-2 GDR-C records were downloaded from the AVISO data archive at http://www.aviso.oceanobs.com. The EGM-08 1′ x1′ geoid was downloaded from http://earth-info.nga.mil/GandG/wgs84/gravitymod/egm2008/oceano.html. The Danish Space Center Mean Sea Surface 2008 (DNSCMSS08) at 1′x1′ was downloaded from http://www.space.dtu.dk/english/Research/Scientific_data_and_models/downloaddata. The SOSE output was downloaded from http://sose.ucsd.edu/sose_stateestimation_data_08.html. The AAO index is from the NOAA Climate Prediction Center and downloaded from http://www.cpc.ncep.noaa.gov/products/precip/CWlink/daily_ao_index/aao/aao.shtml. The authors would like to thank M. Mazloff for his help in using the SOSE data, and three anonymous reviewers and the Editor for their helpful comments on earlier drafts of this paper.

References

Andersen, O. B., and P. Knudsen (2009), DNSC08 mean sea surface and mean dynamic topography models, *J. Geophys. Res.*, *114*, C11001, doi:10.1029/2008JC005179.

Antonov, J. I., R. A. Locarnini, T. P. Boyer, A. V. Mishonov, and H. E. Garcia (2006), Salinity, NOAA Atlas NESDIS 62, in *World Ocean Atlas 2005*, vol. 2, edited by S. Levitus, 182 p., U.S. Gov. Print. Off., Washington, D. C.

Bergmann, I., and H. Dobslaw (2012), Short-term transport variability of the Antarctic Circumpolar Current from satellite gravity observations, *J. Geophys. Res.*, *117*, C05044, doi:10.1029/2012JC007872.

Bingham, R. J., P. Knudsen, O. Andersen, and R. Pail (2011), An initial estimate of the North Atlantic steady-state geostrophic circulation from GOCE, *Geophys. Res. Lett.*, *38*, L01606, doi:10.1029/2010GL045633.

Böning, C. W., A. Dispert, M. Visbeck, S. R. Rintoul, and F. U. Schwarzkopf (2008), The response of the Antarctic Circumpolar Current to recent climate change, *Nat. Geosci.*, *1*, 864–869, doi:10.1038/ngeo362.

Bonin, J. A., and D. P. Chambers (2011), Evaluation of high frequency oceanographic signal in GRACE data: Implications for de-aliasing, *Geophys. Res. Lett.*, *38*, L17608, doi:10.1029/2011GL048881.

Cadden, D. D. H., B. Subrahmanyam, D. P. Chambers, and V. S. N. Murty (2009), Surface and subsurface geostrophic current variability in the Indian Ocean from altimetry, *Mar. Geod.*, *32*, 19–29, doi:10.1080/01490410802661955.

Chelton, D. B., J. C. Ries, B. J. Haines, L. Fu, and P. S. Callahan (2001), *Satellite Altimetry, Satellite Altimetry and Earth Sciences: A Handbook of Techniques and Applications*, chap. 1, Academic Press, San Diego, Calif.

Chereskin, T. K., K. A. Donohue, D. R. Watts, K. L. Tracey, Y. L. Firing, and A. L. Cutting (2009), Strong bottom currents and cyclogenesis in Drake Passage, *Geophys. Res. Lett.*, *36*, L23602, doi:10.1029/2009GL040940.

Cunningham, S. A., S. G. Alderson, B. A. King, and M. A. Brandon (2003), Transport and variability of the Antarctic Circumpolar Current in Drake Passage, *J. Geophys. Res.*, *108*(C5), 8084, doi:10.1029/2001JC001147.

Donohue, K., E. Firing, and S. Chen (2001), Absolute geostrophic velocity within the subantarctic front in the Pacific Ocean, *Int. WOCE Newsl.*, *36*, 12.

Ducet, N., P. Y. Le Traon, and G. Reverdin (2000), Global high-resolution mapping of ocean circulation from TOPEX/Poseidon and ERS-1 and −2, *J. Geophys. Res.*, *105*(C8), 19,477–19,498, doi:10.1029/2000JC900063.

Firing, Y. L., T. K. Chereskin, and M. R. Mazloff (2011), Vertical structure and transport of the Antarctic Circumpolar Current in Drake Passage from direct velocity observations, *J. Geophys. Res.*, *116*, C08015, doi:10.1029/2011JC006999.

Fu, L., and D. B. Chelton (2001), *Large-Scale Ocean Circulation, Satellite Altimetry and Earth Sciences: A Handbook of Techniques and Applications*, chap. 2, Academic.

Fyfe, J. C., and O. A. Saenko (2006), Simulated changes in the extratropical Southern Hemisphere winds and currents, *Geophys. Res. Lett.*, *33*, L06701, doi:10.1029/2005GL025332.

Galperin, B., H. Nakano, H.-P. Huang, and S. Sukoriansky (2004), The ubiquitous zonal jets in the atmospheres of giant planets and Earth's oceans, *Geophys. Res. Lett.*, *31*, L13303, doi:10.1029/2004GL019691.

Ganachaud, A., C. Wunsch, M. Kim, and B. Tapley (1997), Combination of TOPEX/POSIEDON data with a hydrographic inversion for determination of the oceanic general circulation and its relation to geoid accuracy, *Geophys. J. Int.*, *128*(3), 708–722, doi:10.1111/j.1365-246X.1997.tb05331.x.

Gille, S. T. (2008), Decadal-scale temperature trends in the Southern Hemisphere Ocean, *J. Clim.*, *21*, 4749, doi:10.1175/2008JCLI2131.1.

Graham, R. M., A. M. deBoer, K. J. Heywood, M. R. Chapman, and D. P. Stevens (2012), Southern Ocean fronts: Controlled by wind or topography?, *J. Geophys. Res.*, *117*, C08018, doi:10.1029/2012JC007887.

Griesel, A., M. R. Mazloff, and S. T. Gille (2012), Mean dynamic topography in the Southern Ocean: Evaluating Antarctic Circumpolar Current transport, *J. Geophys. Res.*, *117*, C01020, doi:10.1029/2011JC007573.

Hallberg, R., and A. Gnanadesikan (2001), An exploration of the role of transient eddies in determining the transport of a zonally reentrant current, *J. Phys. Oceanogr.*, *31*, 3312–3330.

Hallberg, R., and A. Gnanadesikan (2006), The role of eddies in determining the structure and response of the wind-driven Southern Hemisphere overturning: Results from the modeling eddies in the Southern Ocean (MESO) project, *J. Phys. Oceanogr.*, *36*, 2233.
Katsumata, K., and H. Yoshinari (2010), Uncertainties in global mapping of Argo drift data at the parking level, *J. Oceanogr.*, *66*, 553–569.
Knudsen, P., R. Bingham, O. Andersen, and M. Rio (2011), A global mean dynamic topography and ocean circulation estimation using a preliminary GOCE gravity model, *J. Geod.*, *85*(11), 861–879, doi:10.1007/s00190-011-0485-8.
Lebedev, K. V., H. Yoshinari, N. A. Maximenko, and P. W. Hacker (2007), YoMaHa '07: Velocity data assessed from trajectories of Argo floats at parking level and at the sea surface, *IPRC Tech. Note*, *4*(2), 6.
Le Traon, P. Y., and R. Morrow (2001), *Ocean Currents and Eddies, Satellite Altimetry and Earth Sciences: A Handbook of Techniques and Applications*, chap. 3, Academic.
Locarnini, R. A., A. V. Mishonov, J. I. Antonov, T. P. Boyer, and H. E. Garcia (2006), Temperature, NOAA Atlas NESDIS 61, in *World Ocean Atlas* 2005, vol. 1, edited by S. Levitus, 182 p., U.S. Gov. Print. Off., Washington, D. C.
Marshall, G. J. (2003), Trends in the Southern Annular Mode from observations and reanalyses, *J. Clim.*, *16*, 4134–4143.
Marshall, J., and T. Radko (2003), Residual-mean solutions for the Antarctic Circumpolar Current and its associated overturning circulation, *J. Phys. Oceanogr.*, *33*, 2341–2354.
Maximenko, N., P. Niiler, M. H. Rio, O. Melnichenko, L. Centurioni, D. Chambers, V. Zlotnicki, and B. Galperin (2009), Mean dynamic topography of the ocean derived from satellite and drifting Buoy data using three different techniques, *J. Atmos. Oceanic Technol.*, *26*, 1910–1919, doi:10.1175/2009JTECHO672.1.
Mazloff, M. R., P. Heimbach, and C. Wunsch (2010), An eddy-permitting Southern Ocean state estimate, *J. Phys. Oceanogr.*, *40*, 880–899, doi:10.1175/2009JPO4236.1.
McDougall, T. J., and P. M. Barker (2011), Getting started with TEOS-10 and the Gibbs Seawater (GSW) Oceanographic Toolbox, Version 3.0 (R2010a), *SCOR/IAPSO WG127*, *28*, ISBN 978-0-646–55621-5. [Available at www.TEOS–10.org.]
Meijers, A. J. S., N. L. Bindoff, and S. R. Rintoul (2010), Estimating the four-dimensional structure of the Southern Ocean using satellite altimetry, *J. Atmos. Oceanic Technol.*, *28*, 548–568, doi:10.1175/2010JTECHO790.1.
Meredith, M. P., P. L. Woodworth, C. W. Hughes, and V. Stepanov (2004), Changes in the ocean transport through Drake Passage during the 1980s and 1990s, forced by changes in the Southern Annular Mode, *Geophys. Res. Lett.*, *31*, L21305, doi:10.1029/2004GL021169.
Mo, K. C. (2000), Relationships between low-frequency variability in the Southern Hemisphere and sea surface temperature anomalies, *J. Clim.*, *13*, 3599–3610.
Mulet, S., M.-H. Rio, A. Mignot, S. Guinehut, and R. Morrow (2012), A new estimable of the global 3D geostrophic ocean circulation based on satellite data and in-situ measurements, *Deep Sea Res., Part II*, *77–80*, 70–81.
Orsi, A. H., T. Whitworth III, and W. D. Nowlin Jr. (1995), On the meridional extent and fronts of the Antarctic Circumpolar Current, *Deep Sea Res., Part I*, *42*(5), 641–673, doi:10.1016/0967-0637(95)00021-6.
Pavlis, N. K., S. A. Holmes, S. C. Kenyon, and J. K. Factor (2012), The development and evaluation of the Earth Gravitational Model 2008 (EGM2008), *J. Geophys. Res.*, *117*, B04406, doi:10.1029/2011JB008916.
Picot, N., K. Case, S. Desai, P. Vincent, and E. Bronner (2012), *AVISO and PODAAC User Handbook. IGDR and GDR Jason Products, SALP-MU-M5-OP-13184-CN (AVISO), JPL D-21352 (JPL)*, 125 pp., AVISO, Ramonville St-Agne, France.
Piecuch, C. G., K. J. Quinn, and R. M. Ponte (2013), Satellite-derived interannual ocean bottom pressure variability and its relation to sea level, *Geophys. Res. Lett.*, *40*, 3106–3110, doi:10.1002/grl.50549.
Quinn, K. J., and R. M. Ponte (2012), High frequency barotropic ocean variability observed by GRACE and satellite altimetry, *Geophys. Res. Lett.*, *39*, L07603, doi:10.1029/2012GL051301.
Renault, A., C. Provost, N. Sennechael, N. Barre, and A. Kartavtseff (2011), Two full-depth velocity sections in the Drake Passage in 2006—Transport estimates, *Deep Sea Res., Part II*, *58*, 2572–2591, doi:10.1016/j.dsr2.2011.01.004.
Rintoul, S. R., and S. Sokolov (2001), Baroclinic transport variability of the Antarctic Circumpolar Current south of Australia (WOCE repeat section SR3), *J. Geophys. Res.*, *106*(C2), 2815–2832, doi:10.1029/2000JC900107.
Rintoul, S. R., S. Sokolov, and J. Church (2002), A 6 year record of baroclinic transport variability of the Antarctic Circumpolar Current at 140°E derived from expendable bathythermograph and altimeter measurements, *J. Geophys. Res.*, *107*(C10), 3155, doi:10.1029/2001JC000787.
Rio, M.-H., and F. Hernandez (2004), A mean dynamic topography computed over the world ocean from altimetry, in situ measurements, and a geoid model, *J. Geophys. Res.*, *109*, C12032, doi:10.1029/2003JC002226.
Roemmich, D., and J. Gilson (2009), The 2004–2008 mean and annual cycle of temperature, salinity, and steric height in the global ocean from the Argo Program, *Prog. Oceanogr.*, *82*, 81–100, doi:10.1016/j.pocean.2009.03.004.
Stammer, D., and C. Wunsch (1994), Preliminary assessment of the accuracy and precision of TOPEX/POSEIDON altimeter data with respect to the large-scale ocean circulation, *J. Geophys. Res.*, *99*(C12), 24,584–24,604.
Sun, C., and D. R. Watts (2001), A circumpolar gravest empirical mode for the Southern Ocean hydrography, *J. Geophys. Res.*, *106*(C2) 2833–2855.
Tapley, B., J. Ries, S. Bettadpur, D. Chambers, M. Cheng, F. Condi, B. Gunter, Z. Kang, P. Nagel, and R. Pastor (2005), GGM02—An improved Earth gravity field model from GRACE, *J. Geod.*, *79*(8), 467–478, doi:10.1007/s00190-005-0480-z.
Tapley, B. D., et al. (1994), Precision orbit determination for TOPEX/POSEIDON, *J. Geophys. Res.*, *99*(C12), 24,383–24,404.
Tapley, B. D., D. P. Chambers, S. Bettadpur, and J. Ries (2003), Large scale ocean circulation from the GRACE GGM01 Geoid, *Geophys. Res. Lett.*, *30*(22), 2163, doi:10.1029/2003GL018622.
Thompson, D. W. J., and J. M. Wallace (2000), Annular modes in the extratropical circulation. Part I: Month-to-month variability, *J. Clim.*, *13*, 1000–1016.
Vivier, F., K. A. Kelly, and M. Harismendy (2005), Causes of large-scale sea level variations in the Southern Ocean: Analyses of sea level and a barotropic model, *J. Geophys. Res.*, *110*, C09014, doi:10.1029/2004JC002773.
Whitworth, T., III (1983), Monitoring the transport of the Antarctic Circumpolar Current at Drake Passage, *J. Phys. Oceanogr.*, *13*, 2045–2057.
Whitworth, T., III, and R. G. Peterson (1985), Volume transport of the Antarctic Circumpolar Current from bottom pressure measurements, *J. Phys. Oceanogr.*, *15*, 810–816.
Wunsch, C., and E. M. Gaposchkin (1980), On using satellite altimetry to determine the general circulation of the oceans with application to geoid improvement, *Rev. Geophys.*, *18*(4), 725–745.

Appendix B

Chapter 3 - Article

AGU PUBLICATIONS

JGR

Journal of Geophysical Research: Oceans

RESEARCH ARTICLE

10.1002/2016JC011956

Mapping error in Southern Ocean transport computed from satellite altimetry and argo

Michael Kosempa[1] and Don P. Chambers[1]

[1]College of Marine Science, University of South Florida, St. Petersburg, Florida, USA

Key Points:
- This study quantifies the uncertainty in mapping zonal geostrophic transport of the Antarctic Circumpolar Current
- We show there are significant correlations between the baroclinic and barotropic error contributions to the total transport error
- We show the increase in Argo floats in the Southern Ocean is effective in reducing mapping error

Correspondence to:
M. Kosempa,
mkosempa@mail.usf.edu

Citation:
Kosempa, M., and D. P. Chambers (2016), Mapping error in Southern Ocean transport computed from satellite altimetry and argo, *J. Geophys. Res. Oceans*, *121*, 8063–8076, doi:10.1002/2016JC011956.

Received 9 MAY 2016
Accepted 13 OCT 2016
Accepted article online 18 OCT 2016
Published online 6 NOV 2016

Abstract In an effort to better estimate transport dynamics in response to wind forcing (primarily the Southern Annual Mode), this study quantifies the uncertainty in mapping zonal geostrophic transport of the Antarctic Circumpolar Current from sparse temperature, salinity and sea surface height observations. To do this, we sampled an ocean state estimate at the locations of both Argo floats and the Jason-1 altimeter groundtrack. These sampled values were then optimally interpolated to create SSH and temperature/salinity grids with 1° resolution. The temperature, salinity and SSH grids were then combined to compute the zonal geostrophic transport and compared to that estimated from the full state estimate. There are significant correlations between the baroclinic and barotropic error contributions to the total transport error. The increase in Argo floats in the Southern Ocean is effective in reducing mapping error. However, that error improvement is not uniform. By analyzing systematic errors in transport time series, we find the transects that are most appropriate for analyzing the dynamics of ACC transport using Argo and altimetric gridded fields. Based on our analysis, we conclude region south of Tasmania is most appropriate, with lowest uncertainty. Using real-world data, we calculated zonal transport variability at a transect south of Tasmania. There is an insignificant trend (0.3 ± 0.4 Sv yr^{-1}, 90% confidence) but significant low-frequency variability correlated with the Southern Annular Mode (0.53, $p < 0.05$). The barotropic component is most responsible for the low-frequency variability, and this would be unobservable from ship casts without velocity measurements at depth.

1. Introduction

Increasing winds associated with changes in the Southern Annular Mode are expected to force a response from the Antarctic Circumpolar Current (ACC). Coarse-resolution models have predicted a steepening of isopycnals with increased winds, resulting in an increase in ACC transport [*Fyfe and Saenko*, 2006; *Gnanadesikan and Hallberg*, 2000]. Eddy-permitting models, alternatively, predict an "eddy saturation" that steepening of isopycnals will release the potential energy contained therein as baroclinic eddies [*Hallberg and Gnanadesikan*, 2006, *Meredith et al*. 2012, *Morrison and Hogg*, 2013]. These baroclinic eddies act to reduce isopycnal steepening and retard transport increases. A recent study by *Langlais et al*. [2015] found partial eddy saturation (both transport and eddy energy respond) with increased wind over the ACC, with enhanced eddy kinetic energy lagging behind the wind. Their findings supported the partial eddy saturation predicted by *Farneti et al*. [2010]. A chapter by *Rintoul and Garabato* [2013] provides a review of both theories.

These predicted responses have yet to be unambiguously observed. *Hogg et al*. [2015] found an increase in regional eddy kinetic energy in altimetry data in addition to providing evidence of decreased ACC transport based on sea level around Antarctica. The evidence of transport decrease is supported by observations of decreases in depth-averaged transport computed from data from the Gravity Recovery and Climate Experiment (GRACE) [*Makowski et al*., 2015].

Kosempa and Chambers [2014] calculated zonal geostrophic velocity fields above 1975 dbar for the Southern Ocean from 2004 into 2011. Although other studies have performed similar calculations based on either subsurface T/S from a state estimate or climatology [*Cadden et al*., 2009; *Griesel et al*., 2012] or from projections of surface data onto fixed empirical modes or regressions with historical data [*Meijers et al*., 2010; *Mulet et al*., 2012], *Kosempa and Chambers* [2014] used coincident mapped T/S profiles from Argo and coherent mapping functions for all data sets to reduce problems of using different resolutions. They also used the highest-resolution geoid in processing, unlike other studies [*Cadden et al*., 2009; *Griesel et al*., 2012; *Meijers et al*, 2010].

Kosempa and Chambers [2014] combined Argo-derived densities with surface velocity obtained from Jason-1 and −2 altimetry to estimate zonal geostrophic transport north of 60°S and integrated across much of the ACC. They found a significant correlation between transport variability in the south Indian Ocean and the Southern Annular Mode climate index (Antarctic Oscillation), consistent with correlations seen in the GRACE data [*Bergmann and Dobslaw*, 2012; *Makowski et al*., 2015] and bottom pressure and sea level data in the Drake Passage [*Meredith et al*., 2004]. However, *Kosempa and Chambers* [2014] did not find any significant trend in zonal transport above 2000 dbar in roughly the same region of the south Indian Ocean where *Makowski et al*. [2015] found a strong trend in GRACE-derived transport.

This study was designed to better quantify the error in the method used to derive transport variability in *Kosempa and Chambers* [2014]. Error arises primarily from sampling temperature (T), salinity (S), and sea surface height (SSH) discretely in time and space and objectively mapping in an eddy-rich environment. Their analysis assumed purely random errors and did not quantify potential systematic errors that may arise from mapping sampled data, especially in light of changing numbers of Argo floats in the region over time.

To quantify the error, we relied on output from a high-resolution ocean state estimate—the Southern Ocean State Estimate (SOSE) [*Mazloff et al*., 2010]. We sampled the state estimate at locations and times of individual Argo floats and the along-track Jason-1 and Jason-2 altimetry data, and then optimally interpolated the sampled temperature, salinity, and 5 dbar pressure anomalies (as a proxy of SSH) into gridded fields that are then used to compute geostrophic velocity and transport fields as in *Kosempa and Chambers* [2014]. The optimally interpolated grids were compared to the monthly, 1° averaged values from the full SOSE estimate to quantify uncertainty.

The goals of the experiments are: (1) document the uncertainty for monthly estimates of transport both for 1° gridded and transect-integrated transport; (2) quantify potential systematic errors in transport computed from altimetry and Argo; and (3) identify the areas of the ACC that enable robust observation and analysis of transport dynamics obtained from Argo and satellite altimetry. Section 2 describes the data and methods used. Section 3 presents the results and analyzes the uncertainty. Section 4 discusses the implications of the results in terms of computing trends in integrated zonal geostrophic transport across the ACC.

2. Data and Methods

2.1. SOSE and Sampling

The Southern Ocean State Estimate (SOSE) is a general circulation model solution obtained from the MIT general circulation model (MITgcm) [http://mitgcm.org/]. SOSE assimilates available ocean observations (including altimetry and Argo data) using a least squares estimation technique, with a solution optimized from initial and boundary conditions [*Wunsch and Heimbach*, 2007]. The estimate agrees with observations collected from several platforms and produces a realistic mean zonal transport estimate [*Mazloff et al*., 2010]. The model is eddy permitting at 1/6°, with temperature, salinity and hydrostatic pressure anomaly available at 5 day intervals from 2008 through 2010. SOSE's vertical grid cells spans the full column with 42 levels of varying thickness. The archived "iteration 60" is used throughout this study [http://sose.ucsd.edu/sose_stateestimation_data_08.html]. We restricted latitudinal coverage to between 78°S and 31°S. The pressure anomaly at 5 dbar was chosen as a proxy for altimeter observations of SSH in lieu of the sea surface height available from SOSE. While the products agree at the initial time step, SSH and pressure gradients diverge significantly at late time steps, with pressure gradient being closer with surface velocity obtained from integration of SOSE's internal temperature and salinity. We believe this is most likely due to the fact that the MITgcm uses a free-surface. Since the 5 dbar pressure anomalies should be very close to the geostrophic SSH, we utilize them as a proxy to avoid this significant disparity between the SSH and internal density structure.

A mean monthly climatology was estimated and removed from SOSE T/S prior to sampling, to be consistent with the optimal interpolation (OI) approach used with gridded Argo fields [*Roemmich and Gilson*, 2009]. Because of the SOSE 5 day resolution, months are defined here as 30 day periods, except for 35 days in August. To create climatologies, temperature and salinity state estimates in each 1/6° grid cell were first linearly interpolated to the depth levels used by *Roemmich and Gilson* [2009], except the shallowest layer of SOSE, which remains at 5 dbar. The depth-interpolated temperature, salinity, and pressure anomaly data from SOSE were then averaged over each month and at 1° and retained for comparison with products of

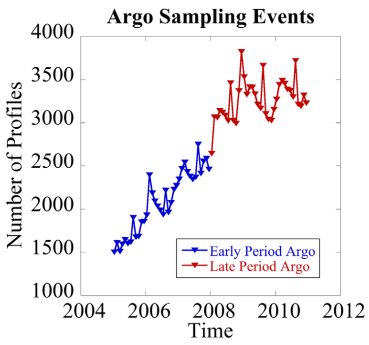

Figure 1. Argo sampling events in the study area (78°S–31°S) binned by month for both the "early" (2005–2007) and "late" (2008–2010) periods.

the optimal interpolation. To produce the final climatologies, a model with annual sinusoids and a linear trend was fit to the 36 month series in each 1° grid by linear least squares. The linear trend was removed from each 36 month series in order to reduce the influence of interannual changes. The resulting de-trended data were averaged for every month to produce the 12 month climatology for each 1° grid and depth level.

The full-resolution SOSE was also sampled to generate T/S profiles at the times and locations of each Argo float, based on historical Argo float sampling locations and times from 2005 through 2010 downloaded from http://www.usgodae.org/cgi-bin/argo_select.pl. SOSE output is only 3 years and so was repeated for the 2005–2007 and 2008–2010 Argo sampling. Only delayed-mode data with a quality control flag of "good" were used. It was assumed T and S was available for all levels to 2000 dbar; although this is not strictly true for many early Argo floats, it is true for late profiles. Thus our computations only consider changes in spatial sampling, not changes in depth sampling. Argo observations in the study area increase from about 1500 per month in early 2005 to over 3000 per month by early 2008, and then hold steady through 2010 (Figure 1).

Full resolution SOSE temperature and salinity fields were interpolated linearly to the geographic locations, standard pressures of *Roemmich and Gilson* [2009], and times of each Argo profile. The resulting sampled SOSE T/S profiles were then aggregated by month. The estimated climatology was then removed to obtain anomalies for use in the optimal interpolation. This was performed for two different periods: 2008 through 2010 (the "full-Argo period") and 2005–2007 (the "transitional-Argo period"). The transitional-Argo period simply sampled the corresponding months of SOSE for 2008–2010.

The altimetry locations and times were derived from a single Jason-1 repeat cycle starting in January 2008 based on the Geophysical Data Records (https://podaac.jpl.nasa.gov/dataset/JASON-1_GDR_NETCDF). To reduce computations in the objective mapping, the times, longitudes, and latitude values were averaged to a 0.5° spacing along-track. The times for the ground track were then repeated every 9.9156 days for 3 years to generate pseudo-SSH locations and times for the period 2008–2010. The full-resolution SOSE pressure anomalies at 5 dbar were then interpolated to these locations/times, and aggregated by month. Colocated values were averaged within each month to save computation. Since the SOSE output is only 3 years and was repeated for the 2005–2007 Argo sampling, we assumed the 2005–2007 SSH sampling was identical to the 2008–2010 sampling. This saved considerable computation time, since we only had to interpolate and map 3 years of pseudo-SSH data.

2.2. Optimal Interpolation and Estimating Geostrophic Currents and Transport

Sampled anomalies of temperature, salinity, and pressure (SSH) were mapped to 1° grids using the same optimal interpolation method and covariance function (C(dist)) as *Roemmich and Gilson* [2009],

$$C(dist) = 0.77\ \exp\left(-\left(\frac{dist}{140.0}\right)^2\right) + 0.23\ exp\frac{-dist}{1111.0}, \quad (1)$$

where dist = sqrt(dx^2 +dy^2), dx is the zonal distance in km between the grid center and observation, and dy is the meridional distance. A noise-to-signal variance ratio of 0.15 was used on the diagonal to account for random noise. The monthly temperature, salinity and pressure anomaly maps were added to their respective climatology to obtain grids of full T, S and SSH.

For analysis of uncertainty, we consider baroclinic, barotropic, and total velocities, where the total is the sum of the barotropic and baroclinic components. We compute these velocities from the 1°, monthly gridding of the full-resolution SOSE data (denoted with the subscript *truth*), and the sampled and mapped data

(denoted with the subscript *mapped*). Thus, the difference between the two (*mapped* – *truth*) indicates the error due to both sampling and mapping.

We use the convention that: baroclinic velocities ($u(z)$) are those derived from the subsurface density assuming a level of no motion at the deepest common level (in this case, 1975 dbar), while the barotropic velocity is the velocity at the deepest level (u(1975 dbar). The total velocity at any depth ($u_{total}(z)$) will therefore be $u(z) + u$(1975 dbar). There are several different ways to compute the baroclinic velocities given density derived from an equation of state [*McDougall and Barker*, 2011]. We use the method of computing dynamic topography relative to 1975 dbar (assuming a level of no motion) for each depth, z, and then computing the velocity from the gradient of the relative dynamic topography. See *Wunsch and Gaposchkin* [1980] or *Kosempa and Chambers* [2014] for a full derivation.

Barotropic velocity (u(1975 dbar)) was derived following the method described in *Kosempa and Chambers* [2014], based on comparing the absolute dynamic topography (ηabs, measured by mapped altimetry) with the relative topography obtained from mapped Argo data (ηrel (1975), integrated from 1975 dbar to 5 dbar)). In our experiment, the absolute dynamic topography is simply the mapped surface pressure anomaly scaled by ($1/g$), where g is acceleration due to gravity. Once the mapped absolute dynamic topography and relative topography are known, the barotropic current can be computed as:

$$u(1975\ dbar) = -\frac{g}{f}\left(\frac{d\eta_{abs}}{dy} - \frac{d\eta(1975\ dbar)_{rel}}{dy}\right). \tag{2}$$

where f is the Coriolis parameter. Errors in the mapped barotropic velocity will arise from errors in both the mapped altimetry and Argo data.

Integrating the velocity data between available levels results in the total volume transport at any location (x,y) and time (t) and its components:

$$\begin{aligned} T(x,y,t)_{baroclinic} &= \int_H^{5\ dbar} u(x,y,z,t)_{baroclinic}\,dz \\ T(x,y,t)_{barotropic} &= \int_H^{5\ dbar} u(x,y,t,H)\,dz. \\ T(x,y,t)_{total} &= T(x,y,t)_{baroclinic} + T(x,y,t)_{baratropic}. \end{aligned} \tag{3}$$

H to refers to the deepest level available at x,y in SOSE. In some cases, this will be shallower than 1975 dbar. Transport (and velocities) will be computed from both the "truth" cases and "mapped" cases and differenced to quantify uncertainty.

2.3. ACC Mask

A persistence measurement [*Kosempa and Chambers*, 2014] was adopted to isolate the ACC region of the Southern Ocean. Persistence is defined as the number of cells in depth and time where the total velocity flowed eastward at each latitude and longitude. For example, a single coordinate (x,y) will have 36*58 = 2088 cells in which there could be eastward flow over the course of 36 months since there are 58 depth levels. ACC persistence was obtained at each latitude and longitude from the 1° averaged SOSE total velocities, and all coordinates with persistence above 94.5% were identified. The ACC was then defined as all cells between the southern and northernmost cells with persistence of at least 94.5% for every longitude (Figure 2).

2.4. ACC Transects

Our definition based on persistence enabled isolation of the ACC for the "mapped" and "truth" grids. However, we also wanted to evaluate transport mapping error across specific transects that are based on those historically sampled by ship casts [http://cchdo.ucsd.edu/]. We identified transects from the database which had been occupied by ships collecting temperature and salinity data after the dawn of altimetry (circa 1993). These transects run roughly perpendicular to the ACC and span its entire breadth as defined by our mask (Figure 2). The collection of temperature and salinity data perpendicular to the ACC allows for computation of baroclinic currents across each transect, which conceivably could be combined with altimetry to add total velocity data points to the time series afforded by Argo. The chosen transects are along the prime

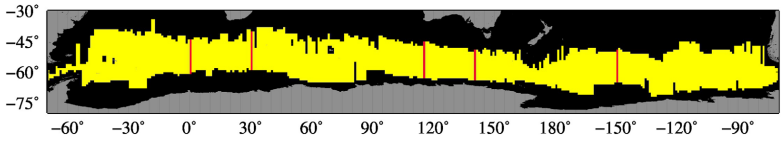

Figure 2. Mask of the ACC, the ACC is shown in yellow. Prime Meridian, Africa, Australia, Tasmania and Pacific transects are indicated in red from left to right.

meridian in the eastern Atlantic Basin, along the 30°E meridian in the western Indian Basin, along the 115°E meridian in the eastern Indian Basin, along the 141°E meridian south of Tasmania and along the 210°E meridian in the Pacific. These transects will be referred to later as Prime Meridian, Africa, Australia, Tasmania, Pacific, respectively.

3. Results

3.1. Velocity Mapping Error (2008–2010)

We first consider the uncertainty in the mapped velocities for the best Argo sampling period (2008–2010) at several levels. For this analysis, we consider the 1° box-averaged data from the full SOSE grids to be the "truth" (or the closest to the truth one can expect), and compute geostrophic velocities at all levels using the surface pressure and T/S data. Likewise, ours is based on the same procedure, but using the mapped surface pressure and T/S from the sampled SOSE data. The impact of aliasing eddies on the optimal interpolation is evident when comparing "mapped" velocities to "truth" at 1975 dbar for a single month (Figure 3). The true barotropic velocities are smoother, with a spatial standard deviation of 2 cm s^{-1}. Despite some high values near bathymetry, extreme values are $\pm$ 5 cm s^{-1} in the "truth" data. The velocities in the mapped data are nearly double this, with a standard deviation of 4 cm s^{-1}.

The mapping error is defined as the standard deviation of the difference between the zonal velocities obtained from the mapped data and those from the "truth" from the averaged full-resolution SOSE data. At 5 dbar, error is due only to mapping of the Jason altimetry data (Figure 4a).The largest errors are located in regions of high mesoscale eddy activity, as expected. Errors are up to 5 cm s^{-1} in the Agulhas and 2–3 cm s^{-1} farther east near 60°E. The mean error over the entire grid shown in Figure 4a is 0.7 cm s^{-1}. Over the area of the ACC defined by our mask (Figure 2) errors are between 2 and 3 cm s^{-1}.

Velocity at depth requires combining the pressure anomaly with subsurface temperature and salinity data from Argo floats. Hence, we expect the mapping error to increase with depth and display geographically similar error patterns as found at the surface (Figure 4b). The average of the zonal velocity mapping error at 1000 dbar grid is double the 5 dbar value, at 1.4 cm s^{-1}. Within the ACC region the errors are between 0.1 and 7.5 cm s^{-1} with an average value of 1.4 cm s^{-1}.

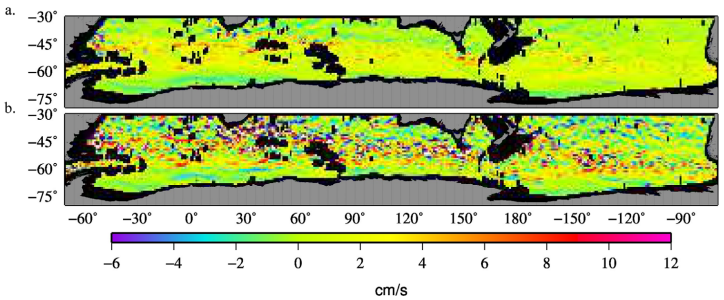

Figure 3. Zonal geostrophic velocity for a single representative month (January 2010) at 1975 dbar using (a) 1° SOSE T/S and pressure anomaly. (b) Argo and Jason-1 and −2 sampling and OI mapped.

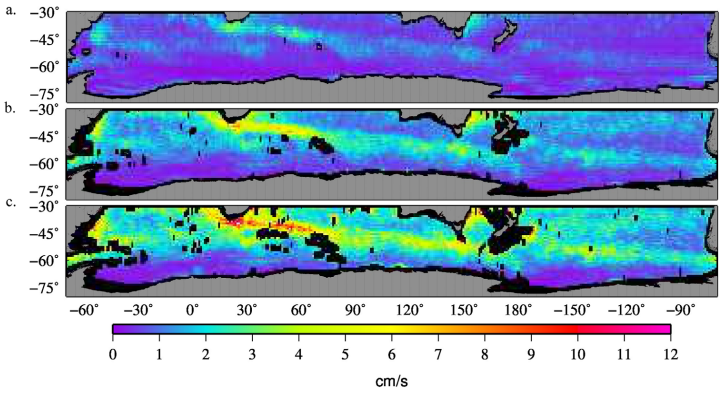

Figure 4. Mapping error in zonal geostrophic velocity at (a) 5 dbar, (b) 1000 dbar, (c) 1975 dbar defined as standard deviation of residuals 2008–2010.

Kosempa and Chambers [2014] estimated the error in the mapped velocity at 1000 dbar by comparing to Argo drifts. Their average error over the entire grid was 2.5 cm s^{-1}, based on an estimate of error in the Argo drift and assuming the errors were uncorrelated. That estimate is considerably higher than what we estimate here. There are several possible explanations for this: (1) the Argo drift velocity error was underestimated, (2) errors in Argo temperature, salinity, and/or depth are significant (they are not considered here), or (3) a combination. Other studies find the errors in temperature, salinity, and/or depth are much smaller than the mapping error [*Roemmich and Gilson*, 2009] which suggests the source of the difference is an underestimation of Argo drift velocity error in *Kosempa and Chambers* [2014].

The mapping error continues to increase with depth to the 1975 dbar level, as shown in Figure 4c). The majority of cells display errors below 4 cm s^{-1} and within the ACC the average error is 2.1 cm s^{-1}. The ACC error is slightly lower than the average of the entire grid (2.2 cm s^{-1}).

3.2. Baroclinic Transport Mapping Error

Mapping errors attributed to baroclinic transport (equation (3)) are routinely less that the barotropic contributions (Figure 5a). The mean uncertainty over the entire grid is 2.0 Sv (1 Sv = 10^6 m^3 s^{-1}). There are values of 7 Sv along the Tasmanian chokepoint, and from 7 to 10 Sv within the Brazil Malvinas confluence. The Indian Basin, particularly close to Australia, displays relatively high baroclinic transport errors (4+ Sv) when compared to the Atlantic (2–3 Sv) and Pacific basins (2 Sv). The average over the ACC is 2.0 Sv. Low values of 1–2 Sv are typical south of the ACC, with the exception of large errors around topographic features.

3.3. Barotropic Transport Mapping Error

Barotropic mapping errors are the dominant source of error (Figure 5b) due to the fact errors in barotropic velocity are high (Figure 4c). These velocity errors are added together at each level without the possibility of cancellation [*Kosempa and Chambers*, 2014]. The mean uncertainty over the entire grid is 4.2 Sv. South of the African continent and east of Australia mapping error exceeds 20 Sv. The area of the Agulhas return has the highest barotropic transport mapping error in the ACC, with values between 20 and 25 Sv. Areas along the Tasmanian and South American chokepoints again demonstrate areas of mapping error between 10 and 15 Sv. These values are again relatively high for the ACC. Most of the ACC, away from the regions south of Africa, have values between 5 and 10 Sv. Barotropic transport error exceeds 7 Sv in the ACC between Africa and New Zealand. For the Atlantic ACC, and areas downstream of New Zealand and upstream of the Drake Passage, the barotropic transport errors are between 3 and 5 Sv. The mean error within the ACC is 4.3 Sv.

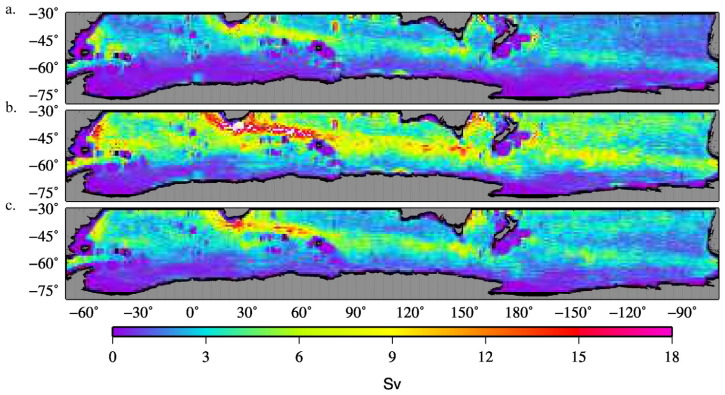

Figure 5. (a) Baroclinic-, (b) barotropic-, (c) total-integrated from depth geostrophic transport mapping error defined as standard deviation of residuals 2008–2010.

3.4. Depth-Integrated Total Transport Mapping Error

The depth-integrated total transport mapping error is shown in Figure 5c. The mean error in the ACC region is 2.7 Sv. The mean mapping error for total transport over the entire grid is 2.6 Sv. A comparison of the total transport error to the means of the baroclinic (2.0 Sv) and barotropic (4.2 Sv) errors suggests significant anti-correlation of errors between the estimated barotropic current and the baroclinic currents, which is what we find (Figure 6). Assuming no correlation from errors (i.e., as done by *Kosempa and Chambers* [2014]), one would assume the error would be 4.7 Sv.

3.5. Mapping Error 2005–2007

The previous analysis was also done for the 2005–2007 sampling period, but we only show the total transport mapping error (Figure 7). The mean over the ACC region is 2.7 Sv. Although the increasing Argo sampling results in improvement in some areas (comparing Figure 5c to Figure 7), that improvement is not uniform. The area with greatest reduction in mapping error is in regions of high eddy kinetic energy, such as the Brazil Malvinas confluence (∼1 Sv improvement) and southeast of the African continent (∼3 Sv improvement). Improvement from increased Argo sampling is also seen along the ACC within the Atlantic and western Indian basins, and at Tasmanian and South American chokepoints. Areas that fail to improve significantly are found along the northern edge of the ACC in the Indian basin, south of Australia within the ACC, and also south of the African continent, which includes the Agulhas retroflection region.

3.6. Transect-Integrated Transport

The ultimate goal of this work is not to measure the transport averaged over a 1° grid, but to integrate it from the south to north across the ACC in order to obtain time-variable transport for any longitude (x) and time:

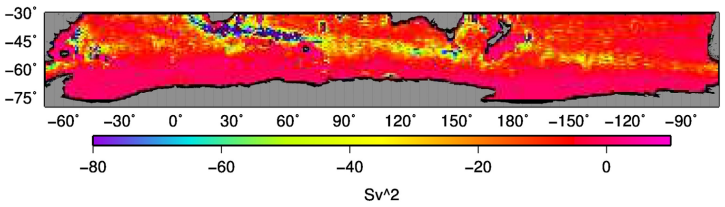

Figure 6. Covariance of barotropic and baroclinic mapping errors.

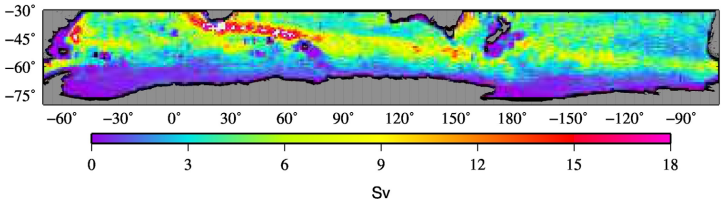

Figure 7. Total integrated transport mapping error for the 2005–2007 Argo sampling period.

$$T(x,t)_{total} = \int_{yS}^{yN} T(x,y,t)_{total} dy. \quad (4)$$

where yS and yN are the south and north boundaries of the ACC as defined by our mask (Figure 2), and vary by longitude.

The longitude-specific transport time-series can also be averaged across meridians to further reduce uncertainty. *Kosempa and Chambers* [2014] estimated that such an averaging would reduce transport errors considerably (by up to 70% in some areas), but they assumed no correlation between local barotropic and baroclinic transport errors, and no correlation between one grid to the next. Here, we can estimate the actual error accounting for correlations, by comparing the transport calculated from the "truth" data with that computed from the "mapped" data. This was done for every 1° of longitude, and after averaging over 11° and 21° of longitude centered on each transect (as suggested by *Kosempa and Chambers* [2014] to reduce uncertainty). Results are shown in Figure 8 for the transect-integrated transport that have 1°, 11°, and 21° averages in longitude centered at every meridian. Correlations between the "truth" and "mapped" transport time-series are high enough to be significant ($p < 0.01$) at every longitude and for every area averaging (Figure 8a).

Mapping error varies with longitude for the three area averages (Figure 8b). Wider area averaging reduces the error at most longitudes. The error is highest south of and down-stream from the African transect, until approximately 70°E when it is 5 – 10 Sv for a 1° transect and 3–5 Sv for a 21°-average. Away from the African transect, the remainder of the ACC has similar mapping error between basins. The characteristic error for 1° transect is approximately 5 Sv, while it is about 3 Sv for 11° and 21° area averaging.

Evolving Argo sampling during 2008–2010 and 2005–2007 periods impacts the mapping error (Figure 8c). For 1° transects, the mapping error is reduced with the 2008–2010 sampling in much of the Atlantic basin

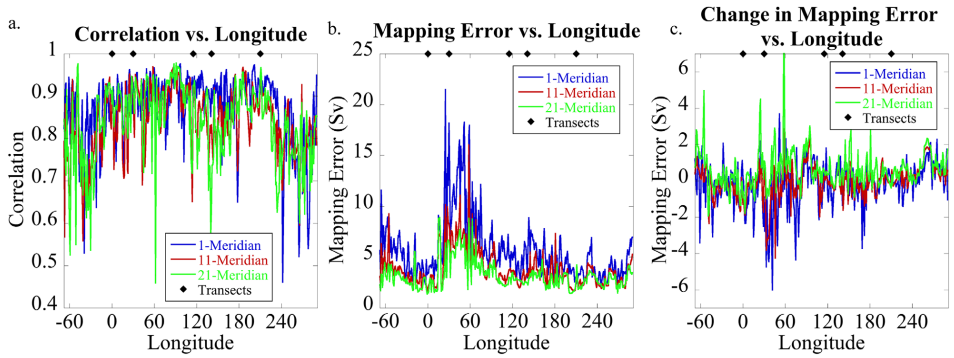

Figure 8. (a) Correlations of mapped and truth total transport time series for the 2008–2010 Argo sampling period (b) total transport mapping error for 2008–2010 mapping period and (c) change in total transport mapping error from 2008–2010 minus 2005–2007 mapping error, i.e., negative values represent an improvement in mapping error. Area averaging was performed after isolating the Antarctic Circumpolar Current based on persistence in each plot.

Table 1. Transect-Integrated Total Transport Mapping Error for Early and Late Argo Sampling Periods at the Prime Meridian, African, Australian, Tasmanian, and Pacific Transects[a]

	Mapping Error 2008-2010 (2005-2007)		
	1 Meridian	11 Meridians	21 Meridians
Prime Meridian	3.51(3.37)	1.54(2.83)	1.53(2.47)
Arica	18.15(19.04)	8.19(7.14)	6.45(7.10)
Australia	4.89(5.45)	3.75(3.60)	3.02(3.23)
Tasmania	4.61(4.36)	3.27(3.34)	2.49(2.69)
Pacific	2.39(2.46)	2.67(2.65)	2.9(3.08)

[a]Results are shown for 1-, 11- and 21- meridian averages for the ACC isolated by persistence.

and that improvement extends until 90° E. The increased sampling after 2008 reduces mapping error most downstream of Africa. A similar improvement is found in the 11° area average. The 21° area average, alternatively, shows little to no improvement for most longitudes, and in some regions, mapping error with the 2008–2010 sampling is worse than with the 2005–2007 sampling, likely indicating more regional degradations in the Argo sampling for these regions as early floats have moved out of the region and not been replaced.

For the 2008–2010 sampling period, the transport error at Africa is 18.2 Sv, but the error at all others is below 5 Sv (Table 1). The lowest transport error is at the Pacific transect (2.4 Sv). After averaging over 11° of longitude, the error at the Prime Meridian transect drops to 1.5 Sv. The Pacific transect error increases slightly to 2.7 Sv. The Australian and Pacific transects errors are 3.8 and 3.3 Sv, respectively. Averaging over 21° of longitude does not significantly reduce error at Africa. Even after averaging over 21°, transport error at Africa is no better than 4.6 Sv.

3.7. Systematic Errors in Transport Variability

This experiment also allows us to estimate systematic errors introduced by the mapping, by examining the transport residuals ($T_{mapped} - T_{truth}$). Because the 11° averaging appears optimal in terms of reducing the mean standard deviation (section 3.6), we only examine those residuals for the 5 historical transects (Figure 9).

Residuals for the two sampling periods at each of the transects described in section 2.4 indicate systematic problems in observation (Figure 9). The Prime Meridian transect's transport residuals show a disparate linear trend at the sampling periods (trends were fit without periodicities by linear least squares). The sampling period 2005–2007 has a trend of 2.18 ± 0.68 (90% confidence) compared to 0.65 ± 0.47 Sv yr^{-1} for the 2008–2010 sampling period. While this indicates the sampling increase is effective in reducing mapping error from early to late sampling periods, the early sampling period would be expected to introduce spurious trends in real-world data. This change could be expected, given the relatively large improvement in mapping error between sampling periods seen in Table 1. The residuals for the African transect are quite noisy, which means any estimated trends are not significant. The residuals for the Australian and Tasmanian transects do not have any significant trends. The residuals for the Pacific transect have large and significant linear trends for both sampling periods (1.48 ± 0.76 Sv yr^{-1} and 1.51 ± 0.76 Sv yr^{-1} at 90% confidence for the early and late sampling periods, respectively). This suggests that transport trends computed from the Pacific transects would likely be overestimated in real world data.

Autocorrelation of the residuals can negatively impact ability to observe transport dynamics (Figure 9). For example, the transport residual at the Australian transect is shown to have a strong, repeating signal. This half-year periodicity in transport error at this location complicates the ability to estimate trends in real-world data and also implies the error estimation in the previous paragraph is too low, as that fitting uncertainty assumes uncorrelated error.

4. Transport Variability From Altimetry/Argo and Evaluation of Trends

Based on the analysis of transect-integrated transport error (section 3.6), and the analysis of the transport residuals (section 3.7), we concluded that the optimal location to study zonal geostrophic transport variability with a combination of altimetry and mapped Argo data is for the Tasmanian transect employing area averaging. Unlike other areas, the area south of Tasmania exhibited no evidence of systematic trends, and nearly random error in addition to the favorably low mapping errors. In addition, the estimated standard error is low (3.3 Sv for an 11-meridian average) and correlation is significant between T_{mapped} and T_{truth} (Figure 8a for 1°, 11° and 21° averages).

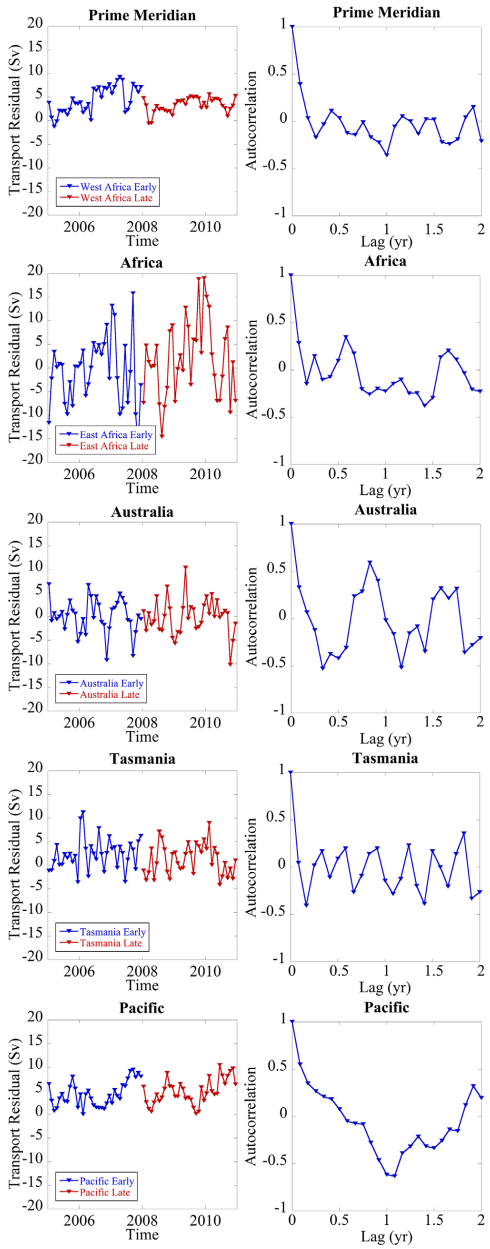

Figure 9. (a–e) Integrated total transport residuals of mapped minus truth 11° averaged transports for the two sampling periods (blue is early (2005–2007), red is late (2008–2010)) and (f–j) Autocorrelation of transport residual at each transect.

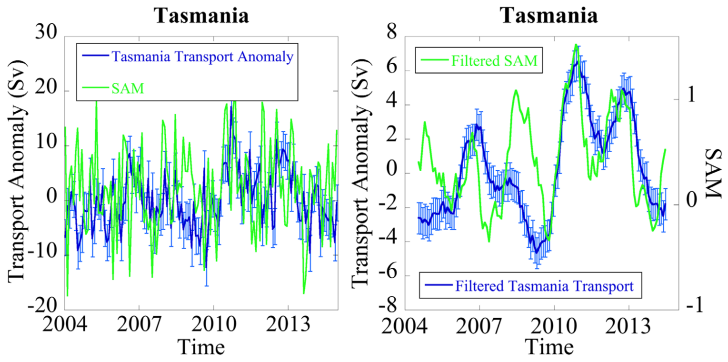

Figure 10. (a) Transport anomaly from real-world observations at the Tasmanian transect and the Southern Annular Mode index (SAM) computed from pressure anomalies at stations [*Marshall*, 2003]. The data were downloaded from http://www.nerc-bas.ac.uk/icd/gjma/sam.html on 26 April 2016. The Tasmania transect's error bars are the mapping errors listed in Table 1. (b) Transport anomaly at Tasmania and SAM after a 13 month low pass filter. Error bars of the 13 month low pass filtered transport time series assume uncorrelated error (that is, 3.3/sqrt(13) Sv).

We calculated the transport anomaly time series for the Tasmanian transect using the mapped Argo data of *Roemmich and Gilson* [2009], and Jason-1 and Jason-2 altimetry data mapped with the same OI function, as outlined in *Kosempa and Chambers* [2014] (Figure 10). The transport was integrated across the ACC based on the persistence measurement in *Kosempa and Chambers* [2014]. An 11° averaging of 1° transects was used. *Kosempa and Chambers* [2014] compared transects near Africa and Tasmania, but found insignificant correlation. That can now be explained by high mapping error in the region south of Africa. The time-series indicates a slight trend over the 10 year time period that is not statistically significant (0.3 ± 0.4 Sv yr^{-1}, 90% confidence). Uncertainty was computed using a Monte Carlo simulation and an AR(1) noise model to represent the serial correlation in the residuals.

Much of the small trend can be explained by the positive transport anomalies throughout 2010–2012 when the Southern Annular Mode (SAM) was also anomalously positive (Figure 10a). It has been demonstrated in several studies that the interannual transport of the ACC is highly correlated with the SAM [e.g., *Meredith*

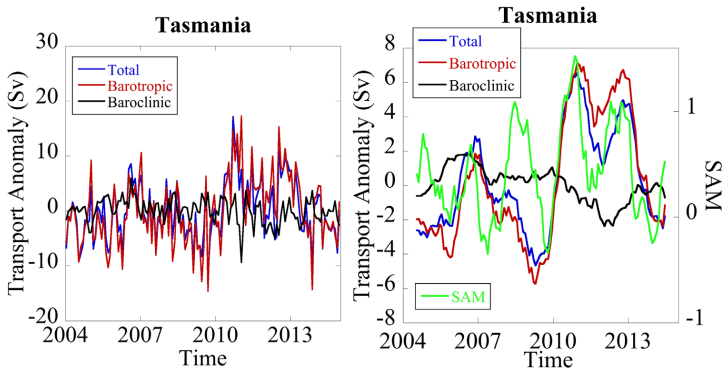

Figure 11. (a) Total, barotropic, and baroclinic transport. (b) Low pass filtered total, barotropic, baroclinic transport.

et al., 2004; *Makowski et al*., 2015]. Although the monthly time series are not significantly correlated (0.1), this is primarily due to different high-frequency signals. If a low-pass filter (13 month boxcar) is applied to both, the correlation improves to 0.53 ($p<0.05$, accounting for reduced degrees of freedom because of smoothing) (Figure 10b).

Deconstructing the total transport observed at Tasmania into barotropic and baroclinic contributions shows the barotropic contribution is the dominant source of variability (Figure 11). The dominance of barotropic variability in response to SAM verifies findings found in *Makowski et al*. [2015]. The total transport and the barotropic contributions are significantly correlated at 0.92, while the total transport and baroclinic contribution are not significantly correlated (Figure 11a). The barotropic and baroclinic contributions display opposing significant trends (0.5 ± 0.4 Sv yr^{-1} versus -0.2 ± 0.1 Sv yr^{-1}, 90% confidence)

5. Conclusions

This study offers a comprehensive uncertainty analysis of volume transport mapped from sparse temperature, salinity, and sea surface height data. We showed the error in the deep current estimated from a combination of altimetry and Argo data is correlated with the baroclinic currents estimated from only Argo, unlike what was assumed by *Kosempa and Chambers* [2014]. The errors are negatively correlated, so combining the deep current and baroclinic currents results in a lower total transport error than considering the barotropic and baroclinic transport errors separately.

This study was also able to quantify the change in mapping error as the Argo program evolved and more floats were put into the Southern Ocean. The change in Argo sampling leads to temporally and regionally dependent errors in several areas (primarily around Africa and in the Pacific). Some of these errors will likely cause significant biases in the transport trends for those regions.

This regional mapping error points to the fact that some areas are better suited for using this technique to analyze transport dynamics than others. The African transect was immediately eliminated from considerations because its error is much higher than the other transects. The Prime Meridian and Pacific transects both indicate significant trend errors within the different Argo sampling periods, and the mapping errors at the Pacific transect are likely nonrandom. That leaves the area south of Tasmanian has having reasonable errors, no evidence of systematic trends, and nearly random error. The Tasmanian transect has the additional benefit of being historically well sampled as a WOCE choke point and has relatively modest eddy kinetic energy as observed by altimetry [*Ducet et al*., 2000].

Our transport time-series captures much of the interannual SAM variability after 2006, but there is a substantial difference in 2008 and 2009, when the estimated transport anomaly is zero or negative but the SAM is positive (Figure 10b). Estimates of transport anomalies from satellite gravity measurements do show increased transport between 2008 and 2009 in this area [*Makowski et al*., 2015], consistent with the SAM. Our analysis indicates the discrepancy between transport and the SAM is not explained by baroclinic transport compensation. The discrepancy could be due to a problem in our transport estimate that has not been captured in our mapping experiment, as no signs of this error are apparent in the residual analysis (Figure 8). The relatively short time series presents another weakness, as there are only 4 cycles of the SAM during the Argo period, and our time series may simply not represent the relationship between low frequency transport anomaly and the SAM. However, more analysis will be needed to quantify the reason. The discrepancy between our transport estimates and the SAM during 2008 and 2009 are directly contributing to disagreement between our trends and those from *Makowski et al*. [2015]. Caveats on SAM disagreement notwithstanding, the response pattern seen in our low frequency time series agrees with the eddy saturation paradigm. While the total transport shows no change in total, the barotropic and baroclinic transport contributions exhibit opposing, significant trends. The increase in barotropic transport results from an increase in dynamic ocean topography gradient at the deepest level of 1975 dbar. Conversely, above 1975 dbar, there is a relaxation of dynamic ocean topography that directly translates into a reduction in depth-dependent transport. If eddies compensating the increased northward Ekman transport are restricted to the upper ocean, the only way for total transport to remain insensitive is a depth-independent response. Therefore, the lack of trend in total transport suggests an ACC transport insensitive to wind increases and also provides evidence for an increase in eddy activity of the upper ocean decreasing dynamic ocean

topography gradients across ACC. A depth-independent response compensates the upper-ocean changes. Further modeling studies could quantitatively test this hypothesis.

Finally, we have also demonstrated that the barotropic variability (i.e., the component due to the reference velocity at depth) is the dominant source of variability, explaining well over 85% of the low-frequency variance that is most correlated with SAM. Using only the density information and assuming a zero velocity at depth (as is typically done with hydrographic sections) would have severely underestimated the transport variability. Thus, understanding and measuring the currents at the deepest common level is critical to measuring the full geostrophic transport variability. Although the method we have investigated as some uncertainty associated with it, as quantified in this study, it is still more accurate than assuming zero velocity at the reference depth. A caveat to this interpretation is the velocity at 2km depth my not be exclusively depth independent and the sensitivity of the definitions presented here require further quantification.

The relatively short instrument record creates another significant drawback of this work. That drawback is the problem of a well-defined climatology, which is crucial for the optimal interpolation and is known to be a concern for the mapping of Argo data in this region [*Roemmich and Gilson*, 2009]. Our experiment assumed a perfect climatology from SOSE. Therefore, our estimates may be slightly optimistic, especially in the early part of the record when the effect of the climatology choice is more pronounced. It is not clear how one would address this problem in the experiment, and with continued Argo observations in the Southern Ocean, this will become less of a problem. A longer instrument record will not only help the climatology but also increase confidence in our trend and correlation analyses.

Another issue is the choice of the southern boundary for mapping of Argo data. *Roemmich and Gilson* [2009], for example, only map data to 60°S. Our ACC mask, however, extends below 60°S in many regions. Our experiments show that the mapping error poleward of 60°S is not higher than areas equatorward (Figure 5). In fact, the errors are smaller, because the largest contribution to the error is sampling of mesoscale eddies. Thus, future mapping of Argo data should extend farther to better encompass the entire ACC.

Even with these caveats, this study verifies that a combination of surface geostrophic currents from altimetry and subsurface density from mapped Argo data can be used to estimate transport variability in the Southern Ocean above 2000 dbar with reasonable accuracy, especially after 2008. These monthly and long-term measurements will supplement in situ estimates made intermittently primarily at the Drake Passage and shed better light on the interannual and decadal variability of the integrated ACC transport.

Acknowledgments
The authors thank Greg Johnson and two anonymous reviewers for their helpful comments in preparing the final version of this paper. This research was carried out under grant number NNX13AG98G from the NASA Ocean Surface Topography Science Team. The Argo data were collected and made freely available by the International Argo Program and the national programs that contribute to it. The Argo program is part of the Global Ocean Observing System. Jason-1 and Jason-2 GDR-C records were downloaded from the AVISO data archive at http://www.aviso.oceanobs.com. The SOSE output was downloaded from http://sose.ucsd.edu/sose_stateestimation_data_08.html. The SAM index is from the British Antarctic Survey (http://www.nerc-bas.ac.uk/icd/gjma/sam.html).

References

Bergmann, I., and H. Dobslaw (2012), Short-term transport variability of the Antarctic Circumpolar Current from satellite gravity observations, *J. Geophys. Res., 117*, C05044, doi:10.1029/2012JC007872.

Cadden, D., B. Subrahmanyam, D. Chambers, and V. S. N. Murty (2009), Surface and subsurface geostrophic current variability in the Indian Ocean from Altimetry, *Marine Geodesy*, *32*(1), 19–29.

Ducet, N., P. Y. Le Traon, and G. Reverdin (2000), Global high-resolution mapping of ocean circulation from TOPEX/Poseidon and ERS-1 and 552 22, *J. Geophys. Res., 105*(C8), 19,477–19,498, doi:10.1029/2000JC900063.

Farneti, R., T. Delworth, A. Rosati, S. Griffies, and F. Zeng (2010), The role of mesoscale eddies in the rectification of the southern ocean response to climate change, *J. Phys. Oceanogr., 40*, 1539–1557, doi:10.1175/2010JPO4353.1.

Fyfe, J. C., and O. A. Saenko (2006), Simulated changes in the extratropical Southern Hemisphere winds and currents, *Geophys. Res. Lett., 33*, L06701, doi:10.1029/2005GL025332.

Gnanadesikan, A., and R. W. Hallberg (2000), On the relationship of the circumpolar current to southern hemisphere winds in coarse-resolution ocean models, *J. Phys. Oceanogr., 30*, 2013–2034, doi:10.1175/1520-0485(2000)030<2013:OTROTC>2.0.CO;2.

Griesel, A., M. R. Mazloff, and S. T. Gille (2012), Mean dynamic topography in the Southern Ocean: Evaluating Antarctic Circumpolar Current transport, *J. Geophys. Res., 117*, C01020, doi:10.1029/2011JC007573.

Hallberg, R., and A. Gnanadesikan (2006), The role of eddies in determining the structure and response of the wind-driven Southern Hemisphere overturning: Results from the modeling eddies in the Southern Ocean (MESO) project, *J. Phys. Oceanogr., 36*, 2233.

Hogg, A. M., M. P. Meredith, D. P. Chambers, E. P. Abrahamsen, C. W. Hughes, and A. K. Morrison (2015), Recent trends in the Southern Ocean eddy field, *J. Geophys. Res. Oceans, 120*, 257–267, doi:10.1002/2014JC010470.

Kosempa, M., and D. P. Chambers (2014), Southern Ocean velocity and geostrophic transport fields estimated by combining Jason altimetry and Argo data, *J. Geophys. Res. Oceans, 119*, 4761–4776, doi:10.1002/2014JC009853.

Langlais C. E., S. R. Rintoul, and J. D. Zika (2015), Sensitivity of Antarctic Circumpolar Current Transport and eddy activity to wind patterns in the Southern Ocean, *J. Phys. Oceanogr., 45*, 1051–1067, doi:10.1175/JPO-D-14-0053.1.

Makowski, J. K., D. P. Chambers, and J. A. Bonin (2015), Using ocean bottom pressure from the Gravity Recovery and Climate Experiment (GRACE) to estimate transport variability in the southern Indian Ocean, *J. Geophys. Res. Oceans, 120*, 4245–4259, doi:10.1002/2014JC010575.

Marshall G. J. (2003), Trends in the southern annular mode from observations and reanalyses, *J. Clim., 16*, 4134–4143, doi:10.1175/1520-0442(2003)016<4134:TITSAM>2.0.CO;2.

Mazloff, M. R., P. Heimbach, and C. Wunsch (2010), An eddy-permitting Southern Ocean State Estimate, *J. Phys. Oceanogr.*, *40*, 880–899, doi: 10.1175/2009JPO4236.1.
McDougall, T. J., and P. M. Barker (2011), Getting started with TEOS-10 and the Gibbs Seawater (GSW) Oceanographic Toolbox, Version 3.0 (R2010a), *SCOR/IAPSO WG127 28*. [Available at www.TEOS-10.org.]
Meijers, A., N. L. Bindoff, and S. R. Rintoul (2011), Estimating the four-dimensional structure of the southern ocean using satellite altimetry, *J. Atmos. Oceanic Technol.*, *28*, 548–568, doi: 10.1175/2010JTECHO790.1.
Meredith, M. P., P. L. Woodworth, C. W. Hughes, and V. Stepanov (2004), Changes in the ocean transport through Drake Passage during the 1980s and 1990s, forced by changes in the Southern Annular Mode, *Geophys. Res. Lett.*, *31*, L21305, doi:10.1029/2004GL021169.
Meredith, M. P., A. C. Naveira Garabato, A. C. McHogg, and R. Farneti (2012), Sensitivity of the overturning circulation in the Southern Ocean to decadal changes in wind forcing, *J. Clim.*, *25*, 99–110, doi:10.1175/2011JCLI4204.1.
Morrison, A. K., and A. McC. McHogg (2013), On the relationship between Southern Ocean overturning and ACC transport, *J. Phys. Oceanogr.*, *43*, 140–148, doi:10.1175/JPO-D-12-057.1.
Mulet, S., M. -H. Rio, A. Mignot, S. Guinehut, and R. Morrow (2012), A new estimable of the global 3D geostrophic ocean circulation based on satellite data and in-situ measurements, *Deep-Sea Research II*, *77–80*, 70–81.
Rintoul, S. R., and A. C. N. Garabato (2013), Dynamics of the Southern Ocean, in *Ocean Circulation and Climate: A 21st Century Perspective*, Int. Geophys. Ser., vol. 103, edited by G. Siedler et al., pp. 471–492, Academic Press, Cambridge, Mass.
Roemmich, D., and J. Gilson (2009), The 2004–2008 mean and annual cycle of temperature, salinity, and steric height in the global ocean from the Argo Program, Prog. *Oceanogr.*, *82*, 81–100, doi:10.1016/j.pocean.2009.03.004.
Wunsch, C., and E. M. Gaposchkin (1980), On using satellite altimetry to determine the general circulation of the oceans with application to geoid improvement, *Rev. Geophys.*, *18*(4), 725–745.
Wunsch, C., and P. Heimbach (2007), Practical global oceanic state estimation, *Physica D*, *230*(1–2), 197–208.